Simulating High-Velocity Clouds in the Observational Plane: An Initial Study with the Smith Cloud

Lori E. Porter,[1]★ Matthew Abruzzo,[2] Greg L. Bryan,[1] Mary Putman,[1] Yong Zheng,[3] and Drummond Fielding[4]
[1]*Department of Astronomy, Columbia University, 538 West 120 Street, New York, NY 10027, USA*
[2]*Department of Physics and Astronomy, University of Pittsburgh, 3941 O'Hara St, Pittsburgh, PA 15260, USA*
[3]*Department of Physics, Applied Physics and Astronomy, Rensselaer Polytechnic Institute, Troy, NY 12180, USA*
[4]*Department of Astronomy, Cornell University, Ithaca, NY 14853, USA*

Accepted XXX. Received YYY; in original form ZZZ

ABSTRACT

High-velocity clouds (HVCs) may fuel future star formation in the Milky Way, but they must first survive their passage through the hot halo. While recent work has improved our understanding of the survival criterion for cloud-wind interactions, few observational comparisons exist that test this criterion. We therefore present an initial comparison of simulations with the Smith Cloud (SC; $d = 12.4$ kpc, $l, b = 40°, -13°$) as mapped with the GALFA-HI survey. We use the Smith Cloud's observed properties to motivate simulations of comparable clouds in wind tunnel simulations with Enzo-E, an MHD code. For both observations and simulations, we generate moment maps, characterize turbulence through a projected first-order velocity structure function (VSF), and do the same for HI column density with a normalized autocovariance function. We explore how initial cloud conditions (such as radius, metallicity, thermal pressure, viewing angle, and distance) affect these statistics, demonstrating that the small-scale VSF is sensitive to cloud turbulence while large scales depend on cloud bulk velocity and viewing angle. We find that some simulations reproduce key observational features (particularly the correlation between column density and velocity dispersion) but none match all observational probes at the same time (the large scales of the column density autocovariance is particularly challenging). We find that the simulated cloud (cloud C) showing growth via a turbulent radiative mixing layer (TRML) is the best match, implying the importance of TRML-mediated cooling for Milky Way HVCs. We conclude by suggesting improvements for simulations to better match observed HVCs.

Key words: ISM: clouds – ISM: individual objects: Smith Cloud – Galaxy: halo – Galaxy: evolution – methods: observational – methods: numerical

1 INTRODUCTION

The accretion of gas onto galaxies, including our own Milky Way (MW), is essential to understand. With our own Galaxy having a current star formation rate (SFR) of a few solar masses per year, a lack of gas accretion could mean that the Milky Way will deplete its gas reservoir in the next billion years if it maintains the current SFR (Chiappini et al. 2001, 2003; Fuchs et al. 2009; Robitaille & Whitney 2010; Chomiuk & Povich 2011; Kennicutt & Evans 2012; Putman et al. 2012; Licquia & Newman 2015; Elía et al. 2022). Therefore, gas accretion is required to provide a continuous source of fuel for the Galaxy's future star formation (Erb 2008; Hopkins et al. 2008; Kennicutt & Evans 2012; Putman et al. 2012; Fox et al. 2019).

As the coldest and densest component of halo gas, high-velocity clouds (HVCs) are thought to be a potential source of future star formation (Oort 1969; Larson et al. 1980; Wakker & van Woerden 1997; Putman et al. 2003; Joung et al. 2012; Putman et al. 2012; Fox et al. 2014; Henley et al. 2017; Fox et al. 2019; Lehner et al. 2022). Hundreds of HVCs have been observed across the entire sky, with many belonging to larger complexes or filamentary structures, and are typically defined by their higher local-standard-of-rest (LSR) velocities ($|v_{\rm LSR}| > 70 - 90$ km/s), or the deviation velocity from Galactic rotation ($|v_{\rm dev}| > 75$ km/s). Due to their ubiquity across the sky, HVCs have a wealth of observational data available at various resolutions (see Wakker & van Woerden 1997; Putman et al. 2012 and references therein for comprehensive reviews).

All potential new Galactic fuel sources, including HVCs, must pass through a galaxy's halo without becoming homogenized with the hot halo, but surviving this passage depends on a wide variety of factors. Because observations of HI structure in these clouds is thought to be evidence that they are moving through the Galaxy's diffuse halo medium and being disrupted (Brüns et al. 2000; Sembach et al. 2003; Putman et al. 2003; Maller & Bullock 2004; Stanimirović et al. 2006; Peek et al. 2007; Putman et al. 2012), the question of whether HVC survive passage through the Galactic halo can be modeled as a cool cloud embedded within a hot medium setup, or "wind tunnel" framework (Heitsch & Putman 2009; Heitsch et al. 2016, 2022; Henley et al. 2017; Bustard & Gronke 2022; Tan et al. 2023).

The generic scenario where a pressure-confined, cool cloud (10^{3-4} K) moves with respect to a coherent hotter ($> 10^6$ K), volume-filling background flow (or "wind") has been studied for decades (McKee & Cowie 1977; Balbus & McKee 1982). It has received significant

★ E-mail: lep2176@columbia.edu

attention in the context of explaining the origin of multiphase galactic outflows, which are commonly composed of comoving cooler and hotter gas phases (e.g Pillepich et al. 2018; Davé et al. 2019). The conventional model holds that supernovae launch hot winds that subsequently accelerate and entrain cool clouds (historically, via ram pressure acceleration) encountered in the ISM as the flow propagates out of the galaxy. However, simulating cloud survival and acceleration has proven remarkably difficult (e.g. Cooper et al. 2009; Scannapieco & Brüggen 2015; Schneider & Robertson 2017; Sparre et al. 2019) because the initial velocity differential drives hydrodynamical instabilities and turbulent mixing that destroys the cloud. A cloud of initial radius $R_{\rm cl}$ is homogenized with a background flow (of speed $v_{\rm w}$ and initial density contrast $\chi = \rho_{\rm cl}/\rho_{\rm w}$) over a few cloud-crushing times $t_{\rm cc} = \chi^{1/2}\frac{R_{\rm cl}}{v_{\rm w}}$ (Klein et al. 1994), which is shorter than the ram pressure acceleration timescale, $\chi\frac{R_{\rm cl}}{v_{\rm w}}$ (Zhang et al. 2017; Abruzzo et al. 2022).

Only recently have simulations been able to model cloud survival in the regime of rapid radiative cooling (Marinacci et al. 2010; Armillotta et al. 2016; Gronke & Oh 2018). Gronke & Oh (2018) showed that when intermediate temperature gas produced by mixing cools sufficiently quickly, mixing acts as a mechanism for transferring mass and momentum to the cloud from the hot phase rather than destroying the cloud. In this regime, the cloud not only survives, but grows. We refer to this process as TRML (turbulent radiative mixing layer) entrainment, a phenomenon whose underlying physics and significance have motivated extensive simulations (e.g. Ji et al. 2019; Fielding et al. 2020; Gronke & Oh 2020a; Tan et al. 2021; Abruzzo et al. 2022; Bustard & Gronke 2022; Chen et al. 2023b; Chen & Oh 2024; Hidalgo-Pineda et al. 2024; Richie et al. 2024).

The criteria for cloud survival has been a topic of debate that largely arises from diverging $\chi \gtrsim 300$ simulation results (e.g Gronke & Oh 2018; Li et al. 2020a; Sparre et al. 2020; Kanjilal et al. 2021; Farber et al. 2022). Abruzzo et al. (2023) resolved this debate by finding that diverging results originated from different choices of cooling functions, whose shapes are known to impact cloud survival (Abruzzo et al. 2022), and proposed a unified survival criterion. The criterion derives from the observation that clouds are destroyed unless they grow, and for a cloud to grow, mixed material originating from the hot phase must be absorbed into the cloud. Thus, mixed hot phase material must cool to the cloud temperature before advecting past the end of the cloud (at which point mixing with the background heats the material back up). This can be restated as $t_{\rm cool,minmix} < \alpha t_{\rm sh}$, where $t_{\rm cool,minmix}$ estimates the characteristic cooling timescale of mixed gas (adapted from Farber et al. 2022) and $\alpha t_{\rm sh}$ estimates the advection timescale. $t_{\rm sh} = R_{\rm cl}/v_{\rm w}$ specifies the time for pristine hot phase material to advect the initial length of the cloud, and α is an empirical constant (∼7) that accounts for the cloud elongation, entrainment, and reduction in speed of hot phase material from mixing. This criterion can be recast as a minimum cloud survival radius, $R_{\rm crit} = v_{\rm w} t_{\rm cool,minmix}\alpha^{-1}$.

Despite new progress in understanding the cloud survival criterion and the relevant physical parameters, many of the quantities in theoretical studies are difficult to determine observationally (Mach number, thermal pressure, etc.). As a result, observational tracers of cloud survival or destruction need to be identified in order to test these criterion on observed clouds. Milky Way HVCs then become ideal probes as their proximity allows detailed spatial and kinematic structure to be observed (Wakker et al. 2002; Ben Bekhti et al. 2009; Hsu et al. 2011).

This motivation has driven various simulations and models of HVCs (Heitsch & Putman 2009; Fraternali et al. 2015; Heitsch et al. 2016; Henley et al. 2017; Bustard & Gronke 2022; Heitsch et al. 2022; Tan et al. 2023). For instance, Bustard & Gronke (2022) investigate survival criterion and TRML in the Magellanic System, predicting that the Leading Arm and part of the trailing Magellanic Stream should survive and even gain mass. Tan et al. (2023) emphasize the importance of gravity, suggesting that survival of HVCs is dependent on the radius of the cloud and dropping height. They predict clouds of height ≤ 10 kpc from the MW to survive their infall, while clouds with larger heights require larger radii to survive (see also Heitsch & Putman 2009; Lehner et al. 2022). While they do not specifically investigate HVCs, Gronke et al. (2022) and Abruzzo et al. (2024) both examine how the velocity structure function (VSF) could be used to characterize turbulence over various length scales ℓ, and further relate the behavior of turbulence to different stages of the cloud survival process.

However, previous studies have been limited in regards to what information can be *directly* used and compared from *both* observations and simulations. In short, there are currently no systematic and comprehensive comparisons of HVCs and simulations in the *observational plane*.

One of the most well-studied Milky Way HVCs is the Smith Cloud (SC). First discovered by Smith (1963), the SC is a relatively large HVC in a high-pressure environment, with the head located at $(l, b) = (40°, -13°)$, and total length of about 20°, inferred to be moving across the sky with an angle of 45° ± 10° (Lockman et al. 2008). Distance estimates for the SC are about 12.4 kpc from the Sun, and within 3 kpc of the Galactic plane, falling towards it at a rate of about $v_z \sim 70$ km s^{-1} (Putman et al. 2003; Lockman et al. 2008; Wakker et al. 2008; Fox et al. 2016). It has a metallicity of half solar (Fox et al. 2016) and an HI mass of $10^6 M_\odot$, with total mass of about $2\times10^6 M_\odot$ (Lockman et al. 2008; Hill et al. 2009). The SC also has an unusually high peak HI column density of $N_{\rm HI} \approx 3\times10^{20}$cm^{-2} compared to most HVCs (peak $N_{\rm HI} \sim 10^{19}$cm^{-2}; Putman et al. 2012). Due to the Smith Cloud's position in the lower halo, it is expected to reflect a surviving cloud.

With the well-constrained properties of the Smith Cloud from new high-resolution GALFA-HI observations and recent advances in simulations of cloud-wind interactions, we present an initial test comparing observed HVCs to simulated (mock observed) clouds in a systematic and consistent manner. In addition, we vary the initial conditions of the simulated clouds, including metallicity, radius, pressure, cloud orientation, and distance in order to determine the effect of each parameter on our measurements. This paper is organized as follows: In Section 2 we outline the GALFA-HI observations, Section 3 details the cloud-wind simulations used, and Section 4 provides an overview of results on observations and mock observations (simulations), including moment maps (4.1), the projected first-order velocity structure function (4.2), the normalized autocovariance function of column density (4.3), and a discussion of how cloud properties may impact these statistics (4.4). We discuss our results and caveats in comparison with previous literature in Section 5, and provide our conclusions and plans for future work in Section 6.

2 OBSERVATIONS

We conduct our observational analysis using data from the Galactic Arecibo L-Band Feed Array HI (GALFA-HI) survey, detailed by Peek et al. (2018). GALFA-HI boasts a high sensitivity and resolution of 4', equivalent to a physical size of approximately 14.4 pc at the distance of the Smith Cloud (12.4 kpc), resulting in the most resolved

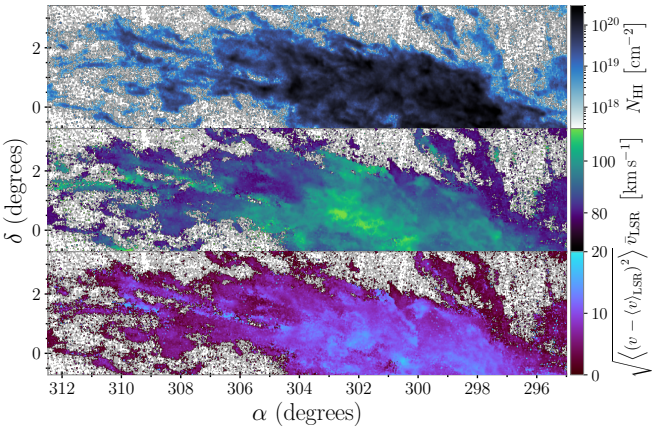

Figure 1. GALFA-HI moment maps of the Smith Cloud, smoothed over 4 km/s in spectral resolution, then integrated across 75-130 km s^{-1} and with a 3σ clipping data reduction. Grey regions represent parts of the observations that are removed by applying the 3σ clipping to brightness temperature before calculating spectral moments. Top row shows the zeroth moment (neutral hydrogen column density; $N_{\rm HI}$), middle row is the first moment (intensity-weighted average $v_{\rm LSR}$), and bottom row is the second moment (intensity-weighted velocity dispersion).

observations of the Smith Cloud (actual size about 1 kpc x 3 kpc) to date.

The GALFA-HI cube of the Smith Cloud has a 0.739 km s^{-1} spacing between velocity channels across a total range of $-68 < v_{\rm LSR} < 188$ km s^{-1}, as used in Holm-hansen et al. (2025). We reduced the velocity range to $75 < v_{\rm LSR} < 130$ km s^{-1}, capturing the majority of Smith Cloud emission while avoiding Galactic contamination. Though we do not show them here, this is confirmed via line profiles. The observations cover the area of the Smith Cloud from $295° < \alpha < 312.5°$ and $-0.725° < \delta < 3.425°$. Due to the limit of the GALFA-HI declination range, we do not capture the entirety of the Smith Cloud, as the main component extends down to $\delta \sim -2°$ (e.g., Lockman et al. 2008), which we address in Section 5.4.

To improve the signal-to-noise ratio, we smooth the observations over 4 km s^{-1} in the spectral dimension. We also employ sigma-clipping with a 3σ limit on brightness temperature when calculating the spectral moments, where σ is taken from an emission-free velocity channel. The observational data after noise reduction is visible in Figure 1, resulting in a minimum column density $N_{\rm HI,min} \approx 3.24 \times 10^{17}$ cm^{-2} and median $N_{\rm HI,med} \approx 2.03 \times 10^{19}$ cm^{-2}.

3 SIMULATIONS

Following Abruzzo et al. (2024), clouds are simulated in a 'wind tunnel' setup by running a suite of 3D uniform grid hydrodynamical simulations using Enzo-E[1], a rewrite of Enzo (Bryan et al. 2014), which is built on the adaptive mesh refinement framework CELLO (Bordner & Norman 2012, 2018).

We conduct four total simulations, named alphabetically as simulations A, B, C and D, respectively. All simulated clouds begin as a slightly perturbed spherical cloud with no initial velocity, embedded within a hot, uniform, laminar wind in the $+\hat{x}$ direction. The cloud and wind are both initialized with the same uniform metallicity. In an attempt to replicate observations of the Smith Cloud, simulation initial conditions are chosen based on observed properties of the SC, described below, though we vary a few parameters between simulations in order to determine how they affect results. Table 1 lists the chosen parameter values for each simulation. All simulations here are run with Mach number $\mathcal{M} = 1.5$, resolution of $R_{\rm cl}/\Delta x = 16$, and density contrast $\chi = 300$, with the exception of simulation D, which has $\chi = 100$. $\mathcal{M} = 1.5$ is implemented for this simulation suite for both observational and theoretical motivations — it corresponds approximately to the observed velocity of the Smith Cloud relative to the sound speed of the hot Milky Way diffuse halo component, and it is often used in cloud-wind studies because it corresponds to transonic outflows observed in galactic winds (Gronke & Oh 2018, 2020a; Farber et al. 2022; Abruzzo et al. 2024; Chen & Oh 2024; Hidalgo-Pineda et al. 2024).

We require that simulated cloud properties obey a simplistic model. The initial cloud temperature is determined by $T_{\rm cl} = f(p, Z_{\rm cl})$, where $f(p, Z_{\rm cl})$ provides the temperature for thermal equilibrium depending on the thermal pressure p and choice of cooling curve, which is determined by cloud metallicity $Z_{\rm cl}$. Then, from the ideal gas law and $\rho_{\rm cl} = n_{\rm cl} m_{\rm H} \mu(p, T_{\rm cl}, Z_{\rm cl})$, where μ is the mean molecular weight and $m_{\rm H}$ is the mass of hydrogen, the density of the cloud is

$$\rho_{\rm cl} = \frac{p\, m_{\rm H} \mu(p, T_{\rm cl}, Z_{\rm cl})}{k_{\rm B} T_{\rm cl}}. \quad (1)$$

Then, because the cloud is initialized as a sphere, the cloud radius is determined by $R_{\rm cl} = \left(\frac{3M_{\rm cl}}{4\pi\rho_{\rm cl}}\right)^{1/3}$.

Properties of the simulated clouds are determined by observations, such as $M_{\rm cl} \approx 10^6 M_\odot$ (Lockman et al. 2008) and $Z_{\rm cl} = Z_\odot/2$ (Fox et al. 2016). As a result, the *only* free parameter we are left with is thermal pressure. Our initial choice of $p/k_B = 10^3$ K cm^{-3} is motivated by this being a standard and reasonable assumption in prior cloud-wind simulations.

Finding that simulations A and B produced lower column densities ($N_{\rm cl}$) than the Smith Cloud prompted us to run simulation C. The relation $N_{\rm cl} \propto n_{\rm cl}^{2/3}$ (from $R_{\rm cl} \propto n_{\rm cl}^{-1/3}$ and $N_{\rm cl} \sim R_{\rm cl} n_{\rm cl}$) motivated our choice of conditions. We initialized simulation C with $p/k_B = 5 \times 10^3$ K cm^{-3}, $T_{\rm cl} = 4430$ K, and $R_{cl} = 169$ pc to maintain mass and metallicity values similar to observations, while producing column densities that are higher by a factor of ≈ 4.

Radiative cooling is modeled with the GRACKLE[2] library (Smith et al. 2017), assuming metallicity estimates of $Z_\odot$ for simulation A and $Z_\odot/2$ otherwise, and no self-shielding. As in Abruzzo et al. (2024), this consists of the tabulated heating and cooling rates for optically thin gas in ionization equilibrium with the $z = 0$ Haardt & Madau (2012) UV background. Radiative cooling in simulations A and B is shut off below the initial cloud temperature of $T_{\rm cl} = 7940$ K, while in simulation C, heating and cooling work normally below the initial cloud temperature, $T_{\rm cl} = 4430$ K. In all simulations, heating and cooling is shut off for $T_{\rm cl} > 0.6 T_{\rm w}$ so that the background medium does not cool.

To determine how radiative cooling — or lack thereof — affects the results, we re-scale the cloud radius, specific internal energy (and by extension, temperature), and thermal pressure of a simulation with no cooling from the suite by Abruzzo et al. (2024) to have the same properties of simulation C, resulting in simulation D. As noted in Abruzzo et al. (2022), we are free to do this due to the self-similarity of the problem in the absence of cooling. We note that

[1] http://enzo-e.readthedocs.io

[2] http://grackle.readthedocs.io

Table 1. Initial conditions (ICs) for each simulation run, including the thermal pressure (p/k_B), radius of the cloud (R_{cl}; chosen such that the mass M_{cl} is $10^6 M_\odot$), metallicity of the cloud (Z_{cl}), temperature and velocity of the wind (T_w, v_w), and density contrast between the cloud and wind ($\chi = \rho_{cl}/\rho_w$). We also include whether the simulated cloud eventually survives, and any additional notes on the particular simulation. Each simulation here has Mach number $\mathcal{M} = 1.5$, resolution of $R_{cl}/\Delta x = 16$, and heating and cooling are shut off for $T_{cl} > 0.6T_w$. From $t_{cc} = \chi^{1/2}\frac{R_{cl}}{v_w}$, one cloud-crushing time is on the order of 10^6 years.

	p/k_B [K cm^{-3}]	R_{cl} [pc]	Z_{cl} [$Z_\odot$]	T_w [K]	v_w [km s^{-1}]	χ	Survival?	Notes
Simulation A	10^3	445	1	1.71×10^6	292	300	Yes	Heating/cooling shut off below T_{cl}
Simulation B	10^3	445	0.5	1.71×10^6	292	300	Yes	Heating/cooling shut off below T_{cl}
Simulation C	5×10^3	169	0.5	7.49×10^5	193	300	Yes	Heating/cooling normal below T_{cl}
Simulation D*	5×10^3	169	0.5	7.49×10^5	111	100**	No	No cooling

*Properties have been re-scaled from an existing simulation in the library from Abruzzo et al. (2024).
** An additional simulation with the same ICs as simulation D, but with $\chi = 1000$, was run to ensure the χ difference compared to $\chi = 300$ of A-C did not result in significant differences. Because the $\chi = 1000$ adiabatic simulation produces comparable observational results to simulation D ($\chi = 100$), we do not show the results here and conclude that this should not affect comparison: a similar $\chi = 300$ adiabatic simulation would have minimal differences with simulation D.

these simulations do not include self-shielding, gravity, or magnetic fields, which we defer to subsequent work and discuss the impacts of in Section 5.4 (see also caveats of Abruzzo et al. 2024).

To project clouds to the observational plane in the form of position-position-velocity cubes, we pick a location to place the cloud relative to the observer, guided by distance estimates for the Smith Cloud from observations (Putman et al. 2003; Lockman et al. 2008; Wakker et al. 2008; Fox et al. 2016). In lieu of a flat-sky approximation and in line with GALFA-HI observations, we construct an array of vectors sampled from a grid of right ascension and declination values, chosen to cover the same region as the GALFA-HI observations, and carry out radiative transfer calculations along each ray, accounting for the local HI density as well as Doppler line broadening from cell temperatures and Doppler shifts due to the component of the velocity along the ray. We estimated the HI density by combining the electron density derived from Grackle's tabulated mean-molecular weight calculations with the assumptions that the gas has a neutral charge and H is as ionized as possible. The resulting image from the plate carrée (or equirectangular) projection is then convolved to have a beam response function to match the GALFA-HI observations.

Once mock observational cubes are produced, we add Gaussian noise ($\mu = 0$ K, $\sigma = 0.08$ K) that roughly approximates the noise in the smoothed Smith Cloud observations over emission-free velocity channels, then smooth the simulations in the same way as observations, over 4 km s^{-1} in spectral resolution. Finally, we implement the same 3σ clipping level on brightness temperature as used for the observations.

4 RESULTS

To make comparisons with the Smith Cloud, we contrast properties that are derived from the SC observations with mock observations of our simulations in identical fashion. We focus on moment maps (and by extension, spatial morphology), velocity structure functions, and normalized autocovariance functions in subsections 4.1, 4.2, and 4.3, respectively. Throughout these subsections, all mock observations were produced in a consistent manner (i.e. consistent orientations and distances). Later, in subsection 4.4, we consider how changing the orientations and distances used to produce mock images alters our results.

To understand the geometric relations between the simulations and mock images used in the first 3 subsections (4.1 - 4.3), it is instructive to reference the panel in the left column of Figure 2 for simulation C, which shows a representative column moment map. The ray between the observer and the center of the simulation domain, which provides data for the mock observation's central pixel at $(\alpha, \delta) = (304°, 1.5°)$, runs parallel to the simulation's z-axis. The distance along this ray is fixed at 12.4 kpc, the observational estimate for the distance of the SC (Putman et al. 2003; Lockman et al. 2008; Wakker et al. 2008; Fox et al. 2016).

We emphasize that the central pixel is the only pixel where the ray along the line of sight (LOS) perfectly aligns with the simulation's z-axis. For example, the ray used to produce the pixel at (312°, 1.5°) lies in the simulation's x-z plane and there is an 8 degree angle (from 312° − 304°) between the ray and the z-axis. We remind the reader that the wind runs parallel to the simulation domain's x-axis, which is orthogonal to the LOS at the center of the image. Plots are oriented such that the wind always enters from the right-hand side, traveling to the left-hand side.

4.1 Moment Maps

4.1.1 Spatial Distributions

To determine physical quantities from the observed and mock observed data cubes, we calculate the spectral moments. Spatial distributions (in sky coordinates α and δ) of the resulting moment maps for the observations are shown in the right column of Figure 1. Here, the Smith Cloud is seen to have it's famous cometary appearance, with the tail of the cloud being visible around $(\alpha, \delta) \approx (310°, 2°)$. Column densities (first row of Figure 1) decrease around the edges of the cloud, and the intensity-weighted mean velocity (second row) appears to increase towards the center, with a large majority of the tail travelling at $\overline{v}_{LSR} \leq 90$ km/s.

Spatial distributions for the simulations at two points in time, $t = 3t_{cc}$ and $t = 12t_{cc}$, are shown in Figures 2 and 3, respectively, where each row represents a simulation and each column is one of the moments. As mentioned, the right ascension and declination range in the mock observations are chosen to match the Smith Cloud observations, and each cloud-crushing time t_{cc} is $\sim 10^6$ years.

In Figure 2, after only a few cloud-crushing times, simulations A (top row) and B (second row) are nearly identical, largely due to the fact that the only differing simulation parameter is metallicity. Even at this early time, though, a contrast can already be seen in the morphology of simulations C and D, which have the same initial radius. Simulation C lengthens as it becomes entrained within the wind, while simulation D decreases in size as it homogenizes with the background flow.

At $t/t_{cc} = 3$, the *maximum* fraction of the gas (by mass) that originated within the cloud is approximately one for all simulations. This indicates that nearly all of the gas mass present is from the

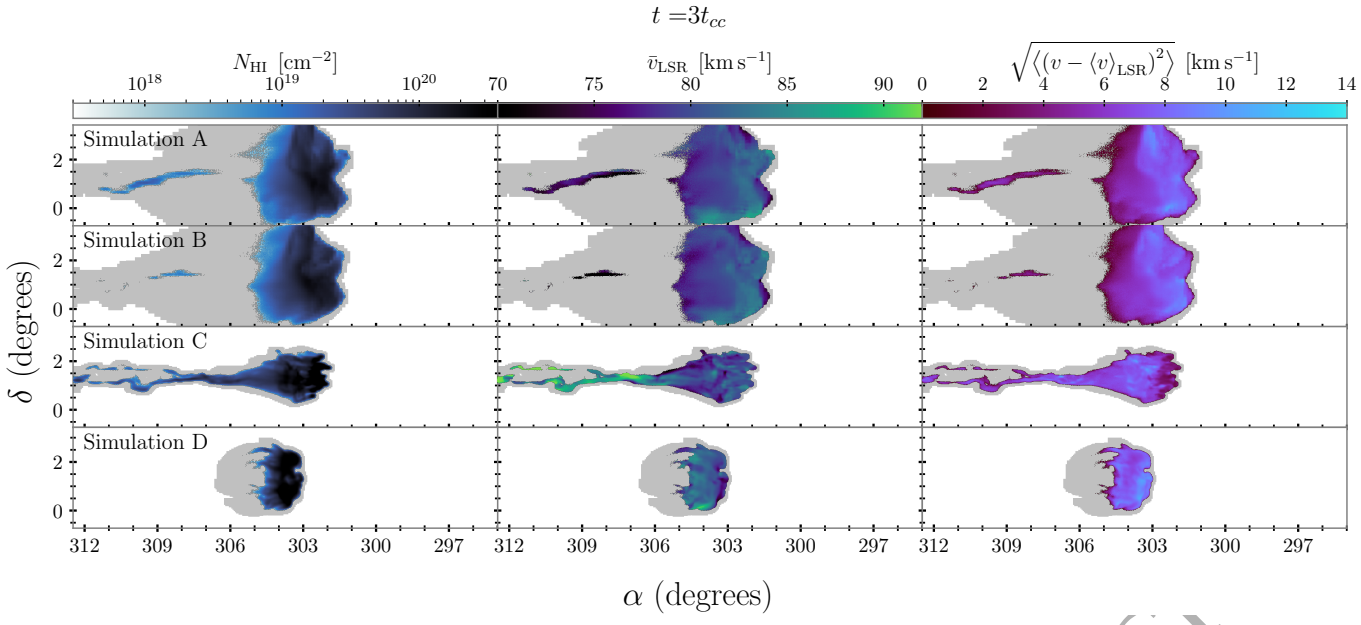

Figure 2. Moment maps of nearly all simulated clouds, with rows organized by simulation and columns by column density (column 1; zeroth moment), intensity-weighted mean velocity (column 2; first moment), and intensity-weighted velocity dispersion (column 3; second moment). All quantities are integrated across the entire simulations' velocity range at $t = 3t_{\rm cc}$. Grey regions represent the entire simulated cloud (without the addition of noise), including data that is removed when applying the 3σ clipping to brightness temperature. Because both simulations C and D are initialized at the same radius, it becomes apparent that simulation D has already begun to become homogenized within the wind, therefore undergoing destruction. We note that these images do not cover the entirety of the simulation volume, and the simulation domain is chosen to minimize boundary effects.

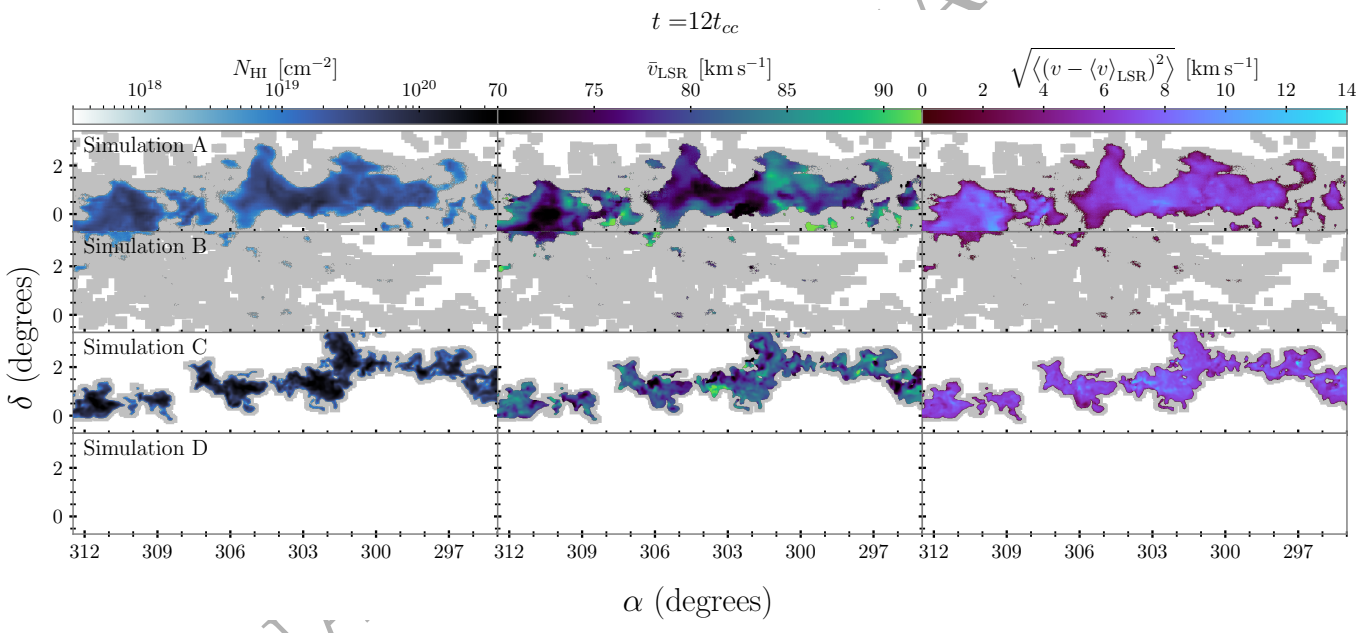

Figure 3. Same as Figure 2, but at $t = 12t_{\rm cc}$. Simulations A and C have been entrained in the wind and are growing, while simulation B has very little visible data. Simulation D does not survive the cloud-wind interaction and is homogenized with the wind (destroyed) by $9t_{\rm cc}$, representing our definition of a destroyed cloud. As in Figure 2, this does not represent the entire simulation volume, but the domain is selected to minimize boundary effects.

initialized spherical cloud, and minimal mass from the wind has been accreted.

At later times in Figure 3, it becomes evident that only simulations A and C have grown, with simulation C doing so at a faster rate than A. Very little of B lies above the observational threshold, though we note it begins growing at times later than $12t_{\rm cc}$. Simulation D, however, has been completely destroyed. Both A and C show clear signs of the filamentary morphology of growing clouds (Cooper et al. 2009; Gronke & Oh 2018).

While Figures 2 and 3 only represent the simulations' spatial dis-

tributions at two distinct cloud-crushing times (of twelve total in this paper), both at different stages of the cloud-wind evolution (pre- and post-entrainment or near/full destruction), it appears that neither are strikingly similar to the Smith Cloud. However, we caution against only using these two cloud-crushing times as the definitive factor for determining whether a good match to the SC is simulated. The SC appears to extend across a range of about three degrees in declination, most similar to simulations A or B in Figure 2, though with column densities and tail structures more reminiscent of simulation C. Noise treatment has some effect on the appearance of the cloud tails, as the tails of A and B are nearly cut out. This indicates that much of the tail of the observed SC is at higher brightness temperatures than some of our simulations. Furthermore, the SC shows the lowest velocity dispersions at the very edges of the visible HI gas structures, and shows a large spread in $\overline{v}_{\rm LSR}$ throughout the cloud, which is more represented by simulation C in Figure 3.

4.1.2 Column Density vs. Velocity

While the the qualitative comparisons of the moment maps' spatial morphology distributions is extremely insightful, it is hard to quantify differences between simulations in different stages of evolution. To make systematic differences easier to see, we examine the joint distributions for pairs of moments (column density, intensity-weighted LOS velocity, and intensity-weighted mean velocity dispersion) that are measured from a given mock observation. With other pairs being discussed in subsequent subsections (see 4.1.3 and 4.1.4), we begin by examining the $N_{\rm HI}$ versus $\overline{v}_{\rm LSR}$ joint distribution in Figure 4.

Colored by the pixel density in each bin, the top panel of Figure 4 shows the joint moment distribution for the Smith Cloud (observational values), which demonstrates a clear trend and appears to be split into two populations: one with distinctly higher velocities and column densities, and one with lower velocities and column densities.

The lower panels of Figure 4 show data measured from the simulated clouds at different times, with rows organized as simulations and columns as specific cloud-crushing times ($t/t_{\rm cc} = 3, 6, 9, 12$). At $3t_{\rm cc}$ (first column), the simulations' LOS velocity measurements seem to span a lower range than the Smith Cloud, especially at the highest column densities. By $6-9t_{\rm cc}$ (second and third columns), the reduced pixel distribution for simulations B and D suggests that the clouds are possibly in the process of being destroyed. At this time for simulation C, however, the LOS velocity measurements span a wider range more comparable to the range of the Smith Cloud.

At $t = 12t_{\rm cc}$ (fourth column), the increasing amount of data illustrates that simulation A starts to rapidly grow, while simulation D is completely destroyed. Simulation C appears to narrow in velocity range, and the column density increases. Simulation B at this time appears to be quite similar to A at $9t_{\rm cc}$, indicating a similar evolutionary stage as the cloud begins to recover and cool enough to be entrained within the wind instead of destroyed.

However, while our mock observations show a similar spread of column densities, none appear to match the Smith Cloud's correlation between the column density and average velocity: instead, mock observed clouds maintain a relatively flat average velocity, particularly at late times as clouds become well-entrained and grow.

As mentioned in Section 4.1, our noise reduction removes both noise and part of the clouds' tails, especially in the lower intensity simulations A and B. This includes more diffuse HI gas, which we observe in a few small areas of the tails to have higher velocities and velocity dispersions than represented by Figures 1 and 2. However, we find that less stringent sigma clipping (e.g., $1-2\sigma$) does not significantly change the distributions displayed by Figure 4 outside of noise, or the joint moment distribution functions discussed in the next subsections. Reducing the restrictive nature of the sigma clipping shows similar primary distributions, albeit with more scatter (of low pixel densities), especially at lower column densities, which is expected due to the nature of the clipping.

4.1.3 Column Density vs. Velocity Dispersion

Figure 5 is similar to Figure 4, but instead shows the joint distribution of column density (zeroth moment) and LOS velocity dispersion (second moment).

The distribution measured from the SC observation maintains a similar cometary morphology to that found in Figure 4, indicating that lower column density gas in the Smith Cloud also has lower velocity dispersions, while the higher column density gas maintains larger velocity dispersions. In addition, the observations form a bimodal distribution: the higher column density distribution appears to be $N_{\rm HI} > 10^{19.75}{\rm cm}^{-2}$, while the lower column density distribution is $N_{\rm HI} < 10^{19.5}{\rm cm}^{-2}$.

In contrast to the the $N_{\rm HI}$ versus $\overline{v}_{\rm LSR}$ plots, the distributions in Figure 5 measured from the mock observations are qualitatively similar to that of the SC. Pixels with larger column density generally have larger LOS velocity dispersions. There are 2 minor exceptions to this trend, both at $t = 3t_{\rm cc}$. First, Simulation C appears to have a small distribution of pixels, separate from the main distribution, at lower velocity dispersion and higher column densities, which disappears at later times. Second, in Simulation D (at this same time), pixels with $N_{\rm HI} > 10^{19.75}$ cm^{-2} have roughly constant velocity dispersions, rather than increasing. We address the reason for the overall similar patterns in 5.1.2.

4.1.4 Velocity vs. Velocity Dispersion

Figure 6 displays the distribution of intensity-weighted LOS velocity (first moment) vs. velocity dispersion (second moment) across the cloud. Similar to Figure 4, the shape of the SC's distribution contrasts that of the simulations at each point in time, whether they are actively growing or being destroyed.

Instead of having a central concentration around a specific velocity and velocity dispersion, the SC's observed distribution retains the cometary (or arc-like) morphology. Much of the gas is concentrated at lower velocities ($\overline{v}_{\rm LSR} \approx 75-90$ km/s) and velocity dispersions, and the velocity dispersion generally increases with increasing velocity.

In the simulations, however, the $\overline{v}_{\rm LSR}$ distribution lacks the clear correlation between LOS velocity and velocity dispersion. Furthermore, many of the simulations have a more clearly defined "center" in their distribution, devoid of the cometary shape.

We find it important to point out that simulations A and B show that clouds may overcome a velocity decline to still grow, contrasting simulation D. In Figure 6, around $6-9t_{\rm cc}$ ($9-12t_{\rm cc}$ for B), the velocity and velocity dispersions both fall, then increase as the cloud is entrained and begins growing. The periods of lower velocities and dispersions are when the clouds' intensities drop from the cloud-wind interaction, but they recover as the cloud cools. During this growing stage, such as simulation A at $12t_{\rm cc}$, the data more closely resemble the joint distribution of simulation C.

We further discuss possible causes behind the discrepancy in simulations and observations in Section 5.

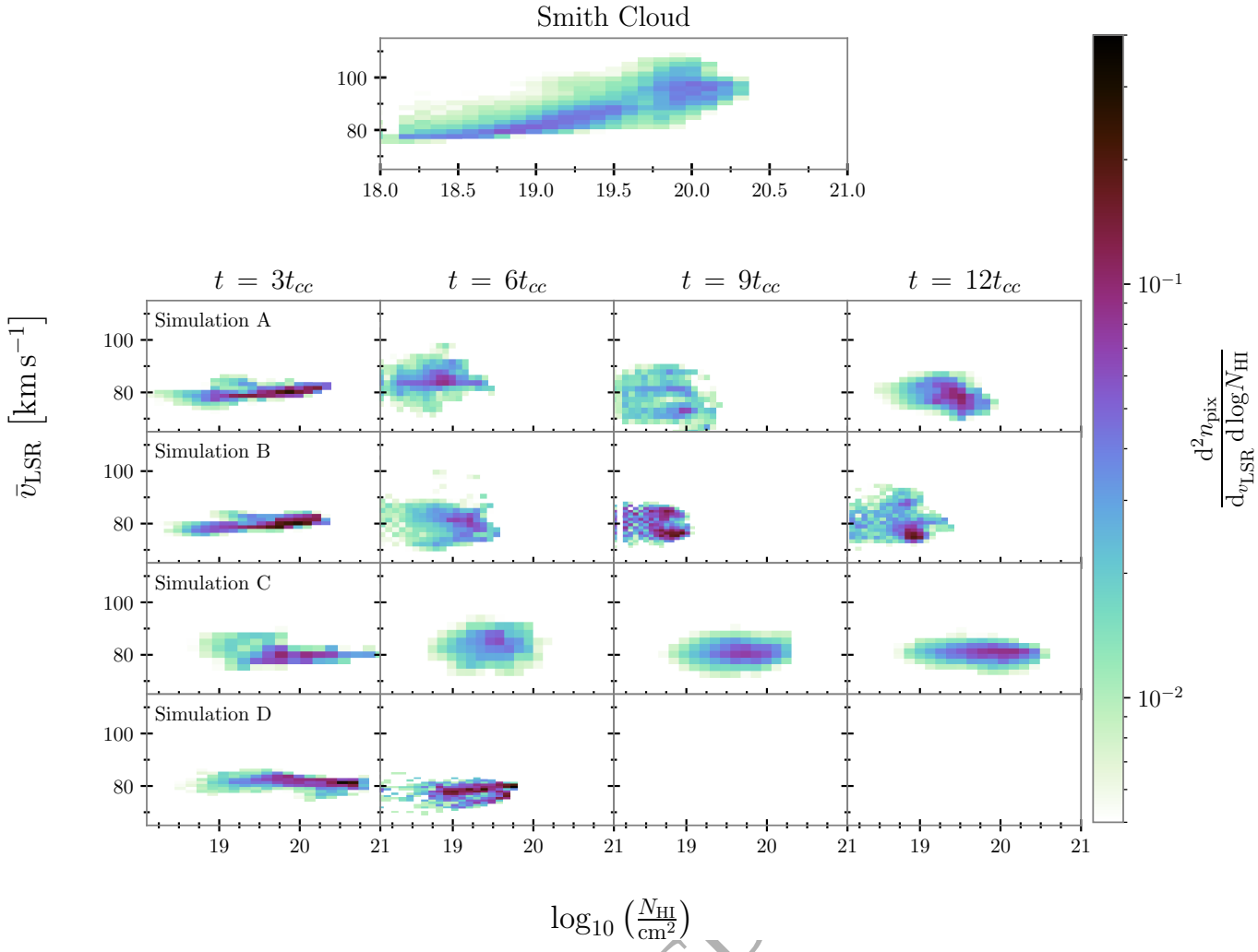

Figure 4. 2-D histograms of column density (zeroth moment) and $\bar{v}_{\rm LSR}$ (first moment) of the Smith Cloud GALFA-HI observations (top panel) and all simulations (lower panels), colored by density of pixels. Rows are organized by simulation, while columns represent different cloud-crushing times. At $3t_{\rm cc}$ (visible in Figure 2), simulations A and B are still identical, while simulation C becomes entrained in the wind, and simulation D is in the process of being destroyed. By $6t_{\rm cc}$, all simulations are diminished except for simulation C. However, simulation A with a metallicity of $Z_\odot$ (therefore more efficient cooling) begins to recover, and starts clearly growing by $12t_{\rm cc}$. Some of B is also visible at this time, and we again note that the mass recovers at a later point in time (see few pixels in Figure 3). Simulation D, our adiabatic run modelled after C, is completely destroyed.

4.2 Projected Velocity Structure Function

To characterize the turbulence within the clouds, we employ the projected first-order velocity structure function (VSF; Frisch 1995). This method characterizes the magnitude of the velocity difference as a function of distance ℓ, computed using $\bar{v}_{\rm LSR}$. Structure functions are useful because theories of turbulence make predictions about how differences in the 3D velocity field vary with ℓ. For example, idealized Kolmogorov turbulence (isotropic, homogeneous, subsonic turbulence in an incompressible fluid) predicts that the velocity scales as $\ell^{1/3}$ up to the length-scale at which the turbulence is driven, where the slope changes (Ossenkopf & Low 2002; Federrath 2013; Chira et al. 2019; Li et al. 2020b; Ha et al. 2021; Gronke et al. 2022; Hu et al. 2022; Li et al. 2023; Abruzzo et al. 2024). However, we note from both Li et al. (2020b) and Mohapatra et al. (2022) that a projected VSF may look somewhat different as a result of the projection effect.

Following Abruzzo et al. (2024), we compute the VSF by defining $|\delta v_\perp|$ as the magnitude of the velocity difference between a pair of randomly-selected points i and j, with the first-order velocity structure function, $\langle|\delta v_\perp|\rangle(\ell)$, being the average value of $|\delta v_\perp|$ for all pairs of points (i, j) from the first moment map (excluding those where $N_{\rm HI} = 0$) separated by a distance of ℓ. We note here that the computed distance is the Euclidean 'pixel' distance using the small-angle approximation and therefore does not account for curvature, though this is unlikely to significantly affect the scales we analyze, and any biases from this approximation would be the same in both the Smith Cloud observations and our mock observations.

Projected first-order velocity structure functions for the observations and all simulations analyzed here are shown in Figure 7. Each column represents the respective simulation, with each output time distinguished by line color. Observations are plotted in each panel as a dashed black line. We require a minimum of 100 pairs of points to be plotted, although this is only relevant in simulations where the clouds are nearly destroyed. Red vertical lines on each panel show the cloud's initial radius, and therefore the initial limit of ℓ, while grey shaded regions are values of ℓ that are not well-resolved accord-

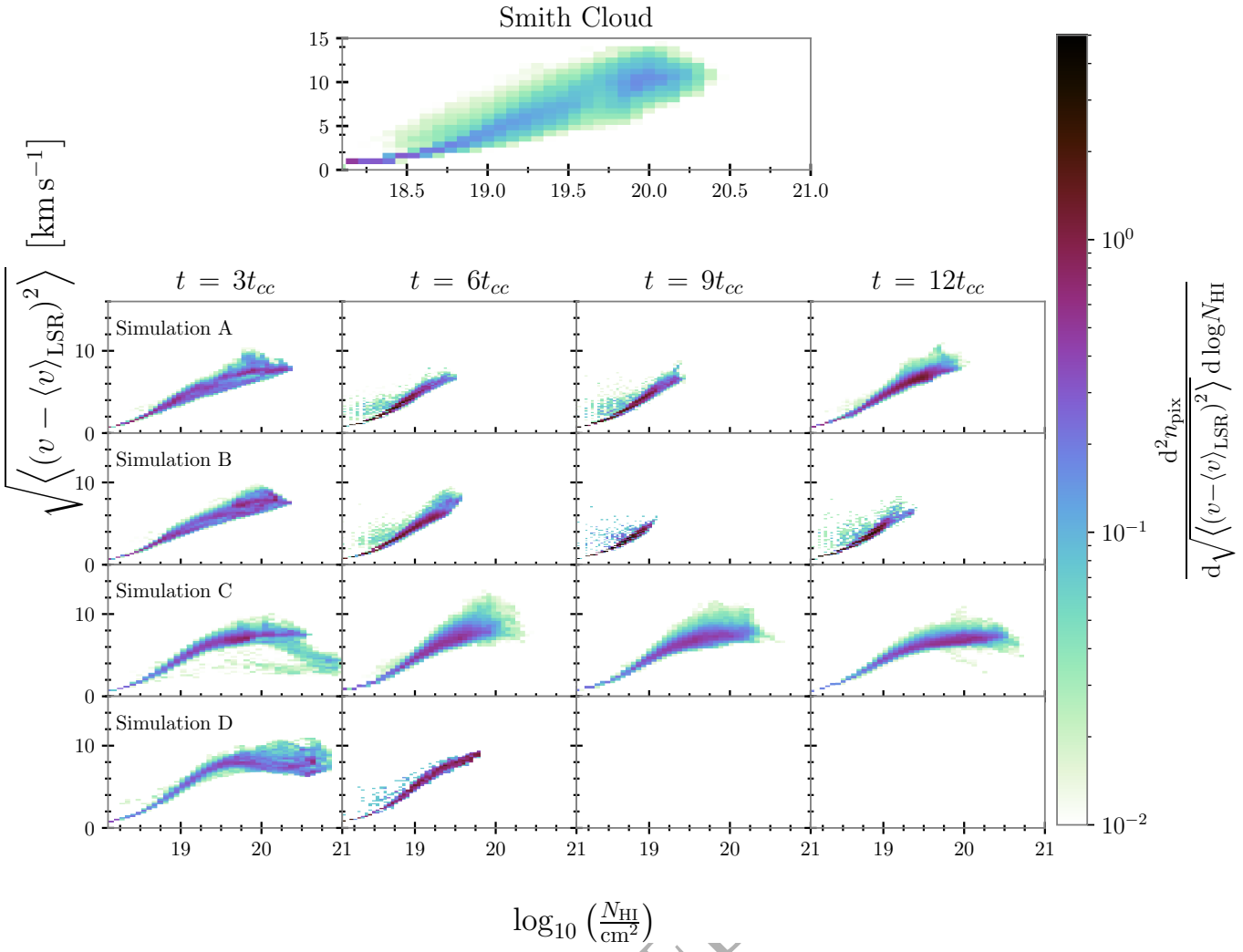

Figure 5. 2-D histograms of column density ($N_{\rm HI}$; zeroth moment) and velocity differences in the cloud ($\sqrt{\langle (v - \langle v \rangle_{\rm LSR})^2 \rangle}$; second moment) in the style of Figure 4. At later times, surviving simulations appear similar to observations, with a cometary shape trailing off to lower velocity differences and column densities. Simulation C, however, is the only simulation that reaches column densities similar to those of the observed Smith Cloud beyond $3t_{\rm cc}$.

ing to the GALFA-HI limit. We also compute second-order velocity structure functions, $\langle |\delta v_\perp|^2 \rangle (\ell)$, but these are qualitatively similar to the first-order structure functions, and therefore we do not show them here.

Despite the differences across the simulated cloud parameters, especially simulation D having no cooling, it is unsurprising that the projected VSFs are so similar at early times in Figure 7. Initially, the cloud has little-to-no turbulence as a nearly uniform sphere at rest. At these early times ($t/t_{\rm cc} < 4$), the clouds all experience an increase in the VSF as turbulence is driven by shear at the cloud-wind boundary, as detailed in Abruzzo et al. (2024). The VSF continues to grow until the cloud is entrained in the wind and the overall velocity difference driving the shear flow drops. This can be seen most clearly in the long-survival run (simulation C). We discuss physical and observational impacts on the VSF in more detail in Section 5.2.

Outside of our unresolved region, many simulations are close to the SC after $3-5t_{\rm cc}$, though A and B experience deviations at higher ℓ as the cloud's intensity falls below our observational limits. Simulation C sees the fewest changes in its VSF after $3t_{\rm cc}$, with increasing time only slightly lowering the magnitude of $\langle |\delta v_\perp| \rangle$. However, the VSF flattens at higher separations (around $\ell \sim 0.15°$). Simulation D is similar to others at early cloud-crushing times, but it does not ultimately survive.

4.3 Normalized Autocovariance Function (ACF)

Just as the VSF provides insight into measures of velocity differences and turbulence across the cloud, we use the normalized autocovariance function (ACF) to do the same for column density.

The normalized autocovariance function is defined as

$$\Gamma(N_{\rm HI}) = \frac{\sum \left(N_{\rm HI}(i) - \langle N_{\rm HI} \rangle\right)\left(N_{\rm HI}(j) - \langle N_{\rm HI} \rangle\right)}{\sum \left(N_{\rm HI}(i) - \langle N_{\rm HI} \rangle\right)^2}, \quad (2)$$

where the summation, similar to the velocity structure function, is over all randomly-selected pairs of pixels (i, j) with separations between separation ℓ and $\ell + \Delta\ell$. Ultimately, this function measures the correlations in the deviation from the mean intensity.

Using this definition, a value of 1 indicates a perfect match in column density between the pair (i, j) (i.e., $N_{\rm HI,i} = N_{\rm HI,j}$), and we

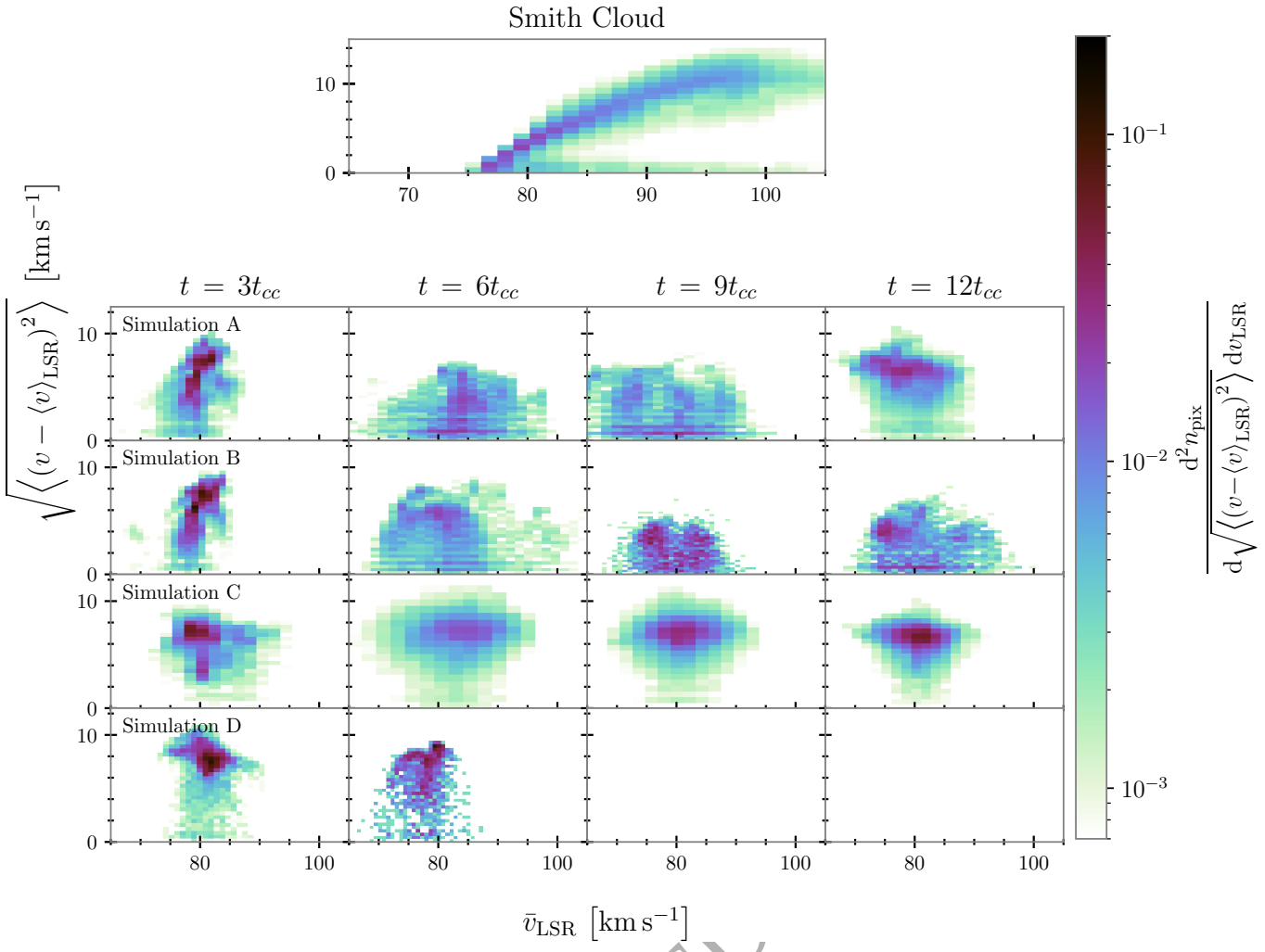

Figure 6. 2-D histograms of $\bar{v}_{\rm LSR}$ (first moment) and velocity dispersion through the cloud ($\sqrt{\langle (v - \langle v \rangle_{\rm LSR})^2 \rangle}$; second moment) in the style of Figure 4. No simulation at any point in time appears to match the morphology of the Smith Cloud observations in this parameter space, but the $6t_{\rm cc}$ column clearly shows how this distribution changes as clouds are either entrained in the wind (simulation C, third row) or homogenized (simulation D, and nearly simulations A and B).

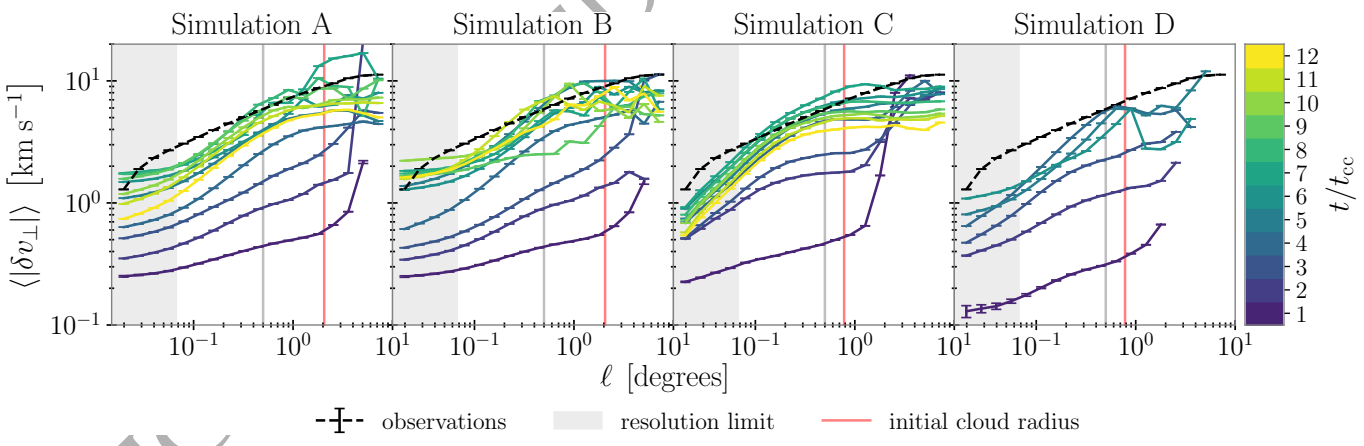

Figure 7. Projected first-order velocity structure functions for each simulation (shown in each column) colored by cloud-crushing time up to $12t_{\rm cc}$. Values measured from the Smith Cloud observations are represented by dashed black lines. We require at least 100 pairs of points in a bin for it to be plotted, and errors are the normalized standard error of the data in that bin. Red vertical lines show the simulated cloud's initial angular size on the sky, while the grey vertical line serves as a point of reference for $\ell = 0.5°$. The shaded grey region for $\ell \leq 0.067°$ denotes the region below the GALFA-HI resolution limit.

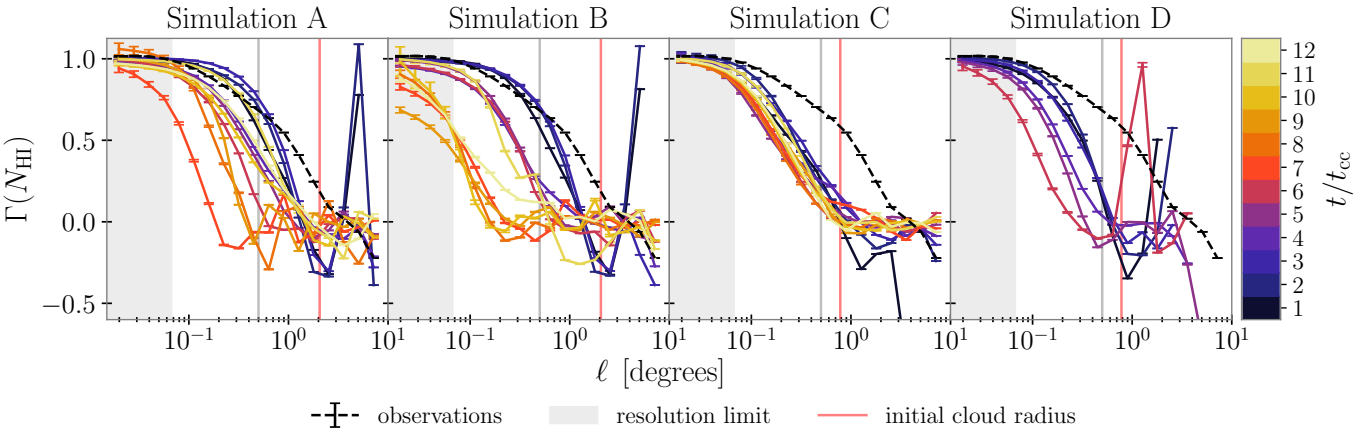

Figure 8. Normalized autocovariance function of column density for each simulation (column) colored by cloud-crushing time up to $12t_{\rm cc}$, similar to Figure 7. Observations are represented by dashed black lines. Errors are the normalized standard error of the data in each bin, where we require at least 100 pairs of points in each bin. Red and grey vertical lines and shaded grey region are as Figure 7. A clear contrast exists between simulations that are being destroyed or growing, as the shrinkage of (nearly) destroyed clouds is evident.

would expect the function to reach zero around the cloud's radius, indicating the size of the cloud. To avoid a dependence on the size of the image, we do not include zeros in this calculation.

Figure 8 shows the ACF for the same set of simulations, again colored by cloud-crushing time. Unlike the VSF, it does not appear that any of our simulations are a strong match to the observations.

All simulations start around $\Gamma(N_{\rm HI}) \approx 1$ on small scales for early cloud-crushing times, similar to the Smith Cloud, as expected. Simulations A and B match the observed slope up to $\ell = 0.5°$ at early cloud-crushing times, beyond which they show a steeper slope. In addition, while simulation C shows slight variations in the function beyond $\ell \approx 0.8°$, it largely flattens to values around 0 (implying no correlation on large scales), which also corresponds to the cloud's initial size as mentioned above.

We note here that adding noise to the simulations and introducing noise reduction effects the function's appearance, explaining the noisy behavior seen in several panels of Figure 8. This is particularly pronounced at larger ℓ values and for clouds that do not survive.

However, we are able to identify possible physical drivers of this measure, which we detail further in Section 5.3. For high-intensity simulations, such as C, the function serve as a possible indication of the cloud size.

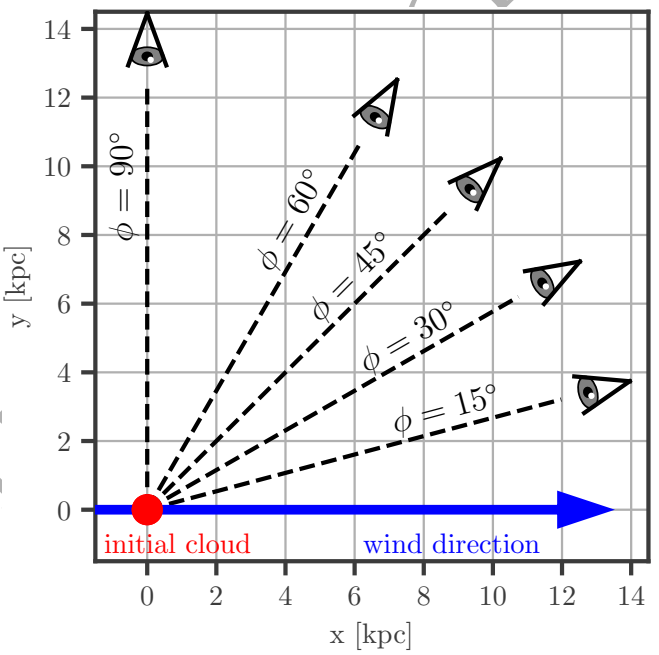

Figure 9. Definition of our viewing angle ϕ. Black dashed lines represent the ray directions for each angle or the line of sight, and the red sphere represents the initial spherical cloud of our simulations. The blue arrow along the +x-axis shows the direction of the hot wind. $\phi = 90°$ corresponds to a viewing angle transverse to the wind.

4.4 Dependence on Cloud Orientation and Distance

Halo clouds have a wide range of distances, from relatively close to the Milky Way's disk in the case of the Smith Cloud, to nearly 100 kpc for the Magellanic Stream, but these distances are often rather uncertain (Wakker et al. 2008; Putman et al. 2012, and references therein). In addition, the viewing angle relative to the cloud motion is rather difficult to constrain. To determine how variations in both viewing angle and distance can affect the statistics we have presented, we vary both properties for simulation C and investigate how (and if) results differ. Simulation C is chosen as it is the cloud that most clearly grows and is consistently above the observational intensity limit, although the trends we find extend to other clouds.

4.4.1 *Varying Cloud Orientation*

While all previous results have used a uniform viewing angle in spherical coordinates of $(r, \theta, \phi) = (d, 90°, 90°)$, where d is the cloud distance, we now keep θ constant at 90° and vary ϕ to 15°, 30°, 45°, 60°, and the previously-shown 90°. The orientation of these viewing angles is visible in Figure 9. The red sphere represents the initial cloud, while the wind travels along the +x-axis, denoted by the blue arrow. The Smith Cloud is predicted by Lockman et al. (2008) to be at a viewing angle of 45° ± 10°.

Figure 10 is similar to Figure 4, displaying 2-D histograms of

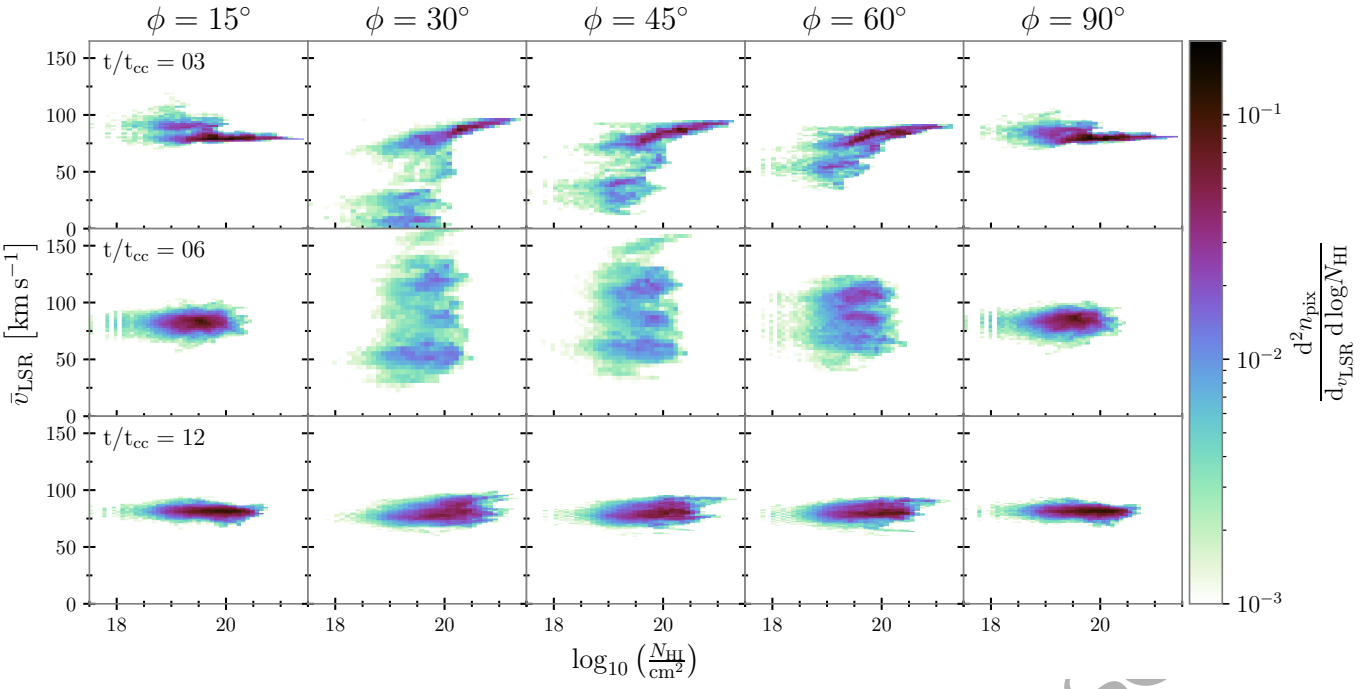

Figure 10. 2-D histograms of column density versus intensity-weighted average velocity, similar to Figure 4, now only for simulation C, and for varying viewing angles relative to the observer; we also note the extended $\overline{v}_{LSR}$ axis compared to Figure 4. Rows represent cloud-crushing times of $3t_{cc}$ (top), $6t_{cc}$ (middle), and $12t_{cc}$ (bottom). Columns are organized by the angle ϕ in spherical coordinates, where we keep θ constant at 90°, as before, and vary ϕ from 15° (first column) up to 90° (last column). The orientation of the cloud appears to only subtly affect column densities at $12t_{cc}$, but significantly affects $\overline{v}_{LSR}$, with $\phi = 30 - 60°$ showing wider velocity ranges of nearly an order of magnitude. This is lessened at the later cloud-crushing time.

column density versus intensity-weighted velocity. However, we now only show results for simulation C, calculated at cloud-crushing times of 3 (top row), 6 (middle row), and 12 (bottom row), and for the specified angles of ϕ (different columns). Despite similarities to Figure 4, we also note the substantially increased dynamic range of the velocity axis (and remind readers that, in the observational case, velocities below about 65 km/s are hard to interpret due to possible confusion with the Milky Way).

For the intermediate angles of $\phi = 30 - 60°$, the range of intensity-weighted velocities increases significantly compared to the previous results from $\phi = 90°$, which have only minute differences from $\phi = 15°$. However, this depends sensitively on the stage of the cloud-wind interaction. When the cloud is early in its interaction with the hot wind, at $3t_{cc}$, $\overline{v}_{LSR}$ for $\phi = 30°$ covers the 0-100 km/s range, the lower limit of which then increases with increasing ϕ, before finally decreasing to the previously observed range of $\approx$ 75 – 100 km/s at $\phi = 90°$. These LOS velocities then become even more widely distributed at $6t_{cc}$ before collapsing into a narrower distribution at $12t_{cc}$, by which time the cloud has been growing for some time and is largely entrained in the wind. While angles of $\phi = 30 - 60°$ at this time still show slightly larger variations in $\overline{v}_{LSR}$ than for $\phi = 15°$ and $\phi = 90°$, the effect is considerably less than at earlier cloud-crushing times. As a result, it appears the physical perspective of $\phi = 90°$ fails to capture the bulk velocity along the length of the cloud, while lower angles become dominated by it.

We note that the shape of the distributions at $t = 3t_{cc}$ and $\phi = 30 - 60°$ appears to be a much better match to the Smith Cloud than at $\phi = 90°$ in Figure 4. In particular, higher column density material for $\phi = 30 - 60°$ also has higher velocities, and the velocity matches the observational range of about 75-100 km/s.

Although we do not show it here, the velocity dispersion varies with viewing angle similarly to the LOS velocity, as expected. However, despite the different orientations, we still do not see a good match for the Smith Cloud's joint distribution of LOS velocity and velocity dispersion (Figure 6).

Finally, the effect of viewing angle on the velocity structure and autocovariance functions of simulation C, at cloud-crushing times up to 12, can be found in Figure 11. Of the two functions, the VSF changes significantly more with ϕ than $\Gamma(N_{HI})$.

The shape of the VSF is significantly different for $\phi = 30 - 60°$, especially at both early times *and* large ℓ.

For these angles ($\ell > 2°$), where the VSF previously flattened to a near-constant value at cloud-crushing times greater than three, it now continues to increase, stretching up to values an order of magnitude higher than $\phi = 0°$ or 90°. As before, $\phi = 30°$ shows the biggest shift, with VSF values decreasing with increasing ϕ until the VSF again flattens at large ℓ for $\phi = 90°$. We find that the intermediate angles of ϕ ($30 - 60°$), particularly at late times, show a better match to the projected VSF of the Smith Cloud.

Larger scales of $\ell > 1°$ are more sensitive to the bulk velocity along the cloud. This is evident across simulations A-D, where simulations undergoing (near) homogenization with the hot wind show larger variation in their VSF, or simply do not reach ℓ larger than that of the cloud's initialized size. This also explains why the velocity structure functions are more sensitive to viewing angle but less so to resolution. The bulk motions of the cloud are generally resolved, but changing the line-of-sight with respect to the cloud and wind allows for a different perspective of the bulk motions driven by the wind in the $+\hat{x}$-direction.

Despite the dependence of the VSF on cloud orientation, the autocovariance function of column density, $\Gamma(N_{HI})$, shows very little quantifiable dependence (bottom row of Figure 11. Again, we note

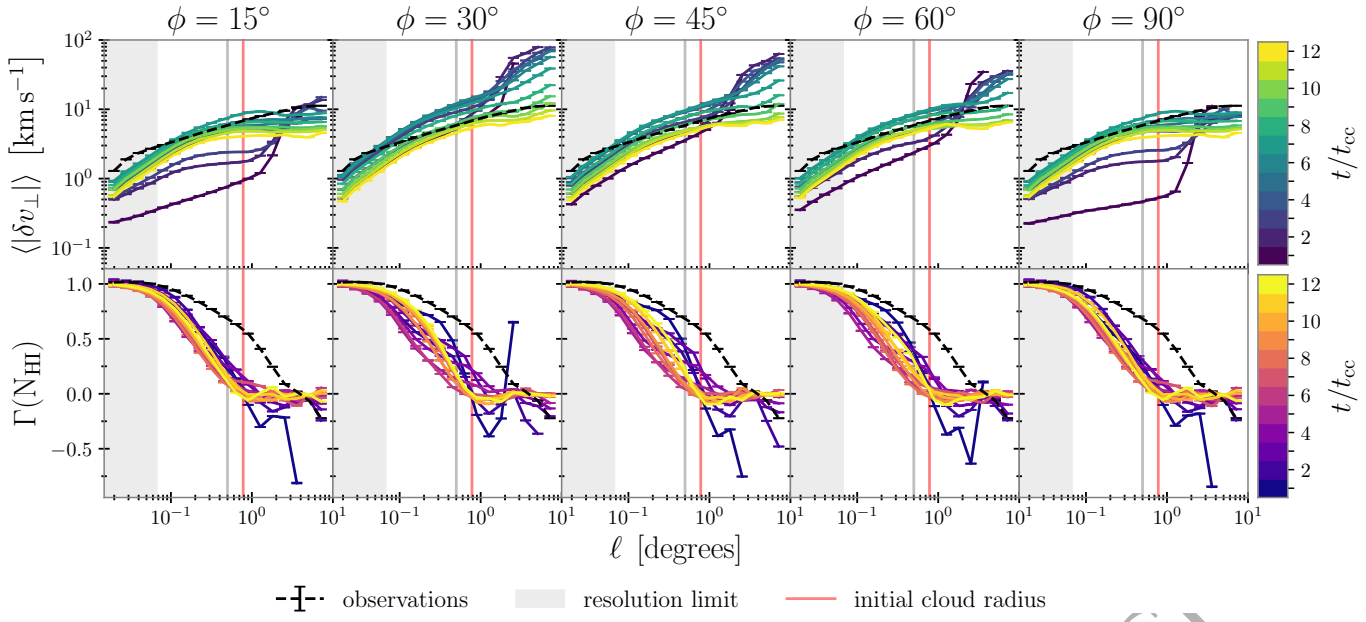

Figure 11. Projected velocity structure function (top row) and normalized autocovariance function of column density (bottom row) of simulation C, for varying cloud orientations ($\phi = 15 - 90°$). Lines are colored by cloud-crushing time, as Figures 7 & 8, respectively. The angle of cloud orientation appears to significantly affect the VSF, with $\phi = 30 - 60°$ showing larger values of $\langle|\delta v_\perp|\rangle$ at earlier cloud-crushing times across all ℓ. In addition, instead of the VSF flattening at larger ℓ, $\phi = 30 - 60°$ result in an increase of $\langle|\delta v_\perp|\rangle$. However, the autocovariance function does not seem to be significantly affected, with only slight variations at low cloud-crushing times, similar to the conclusion from Figure 10.

that the results for angles of $\phi = 15°$ and $\phi = 90°$ are nearly identical. This is unsurprising given that the primary impact of viewing angles appears to be the bulk velocity along the cloud.

4.4.2 *Varying Cloud Distance*

Finally, we turn to cloud distance. Because the joint distributions (2-D histograms) across each set of moments are not significantly impacted by increasing or decreasing the cloud distance, we do not show them here. Instead, Figure 12 shows the VSF (top row) and ACF (bottom row) with a constant viewing angle of $\phi = 45°$, but changing cloud distance. $\phi = 45°$ is chosen here to highlight the variation in both functions with distance, as the effect is considerably more subtle at our initial $\phi = 90°$. The middle column represents the predicted distance of the Smith Cloud from previous literature, $d = 12.4$ kpc, and we scale this distance by $\sim$ 75% to 9 kpc (first column), and $\sim$ 200% to 25 kpc (last column).

Distance does not significantly impact the overall shape of these functions, although slight effects may be seen. Rather, it stretches or compresses the distribution with respect to ℓ. As distance increases, the change in the slope of the VSF decreases to lower ℓ. This behaviour is expected given the relation between angular size and physical distance.

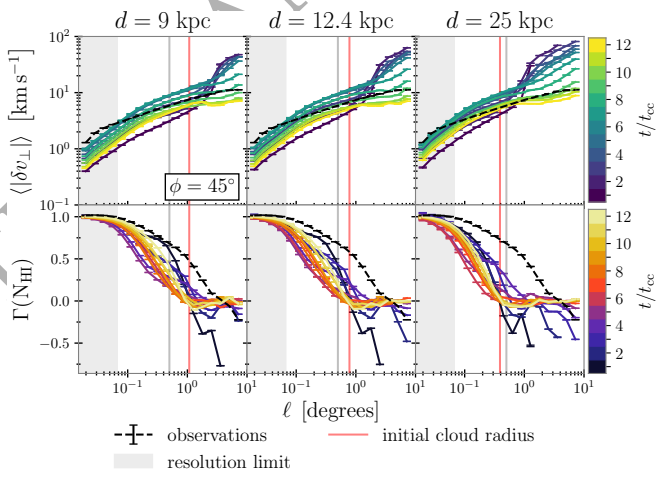

Figure 12. Projected velocity structure function (top row) and normalized autocovariance function of column density (bottom row) for simulation C, but now varying cloud distances (columns) at the same angle of $\phi = 45°$. The middle column represents the observed distance of the Smith Cloud, while the first and second columns are 75% and 200% of this distance, respectively. Red vertical lines show the simulated cloud's initial angular size on the sky, while the grey vertical line serves as a point of reference for $\ell = 0.5°$. The shaded grey region for $\ell \leq 0.67°$ denotes the region below the GALFA-HI resolution limit. Both functions appear to be shifted towards smaller ℓ as distance (and initial angular size) increase.

5 DISCUSSION

Following the presentation of our Smith Cloud GALFA-HI observations and simulated mock observations, we now consider our results in a broader context and compare to previous literature. We first consider whether our simulated (mock observed) clouds match the observed Smith Cloud (5.1), then revisit the physics involved in the velocity structure function (5.2), before turning to possible implications for observers (5.3), and limitations of this study (5.4).

5.1 Can Simulations Reproduce Observations?

We have demonstrated that it is possible to carry out a detailed comparison between mock observations of cloud/wind interactions and radio data cubes, and several individual metrics can be reproduced (or nearly reproduced). We find that all radiative simulations with observationally-motivated properties (A, B, and C) are surviving clouds, with simulations A and C being the closest overall matches to the Smith Cloud, especially when the viewing angle is changed. We further highlight the relevance of TRML entrainment, how metrics shown change with different simulation properties, their physical drivers, and whether they may serve as a diagnostic for cloud survival or destruction. Given the position of the Smith Cloud in the lower halo of the MW, we emphasize that a similar simulated cloud likely needs to be stable against destruction (homogenization with the halo), as we have done here (with the exception of simulation D).

5.1.1 Relevance of TRML Entrainment to HVCs

This paper was designed to study HVCs through TRML entrainment models (and vice versa) with recent high-resolution observations and simulations. While it was previously theorized that TRML entrainment is relevant for HVCs, we have now placed this on firmer observational footing. In particular, given the cloud initial conditions, we find that our best match simulation is the one clearly showing TRML entrainment.

Section 3 outlines the model that simulated initial clouds follow. In short, Equation 1 encodes the basic arguments about cloud properties that result in *highly* constrained initial conditions if we wish to match what has been observed of the Smith Cloud. In fact, because we have observational measurements for the mass $M_{\rm cl}$ and metallicity $Z_{\rm cl}$, the *only* free parameter is thermal pressure (outside of initial cloud velocity and shape). As a result, significantly lowering the thermal pressure is likely the only way that cooling does not significantly alter cloud evolution.

Indeed, the importance of radiative cooling is evident in simulations A and B. Although the only difference between A and B is the lower metallicity, simulation A appears to grow more quickly than B, especially visible in Figure 3. The detailed physics of turbulent radiative mixing layers are then crucial to the cloud's evolution.

5.1.2 Column Density, Velocity, and Velocity Dispersion

We are able to replicate the Smith Cloud's distribution of HI column densities, derived from the zeroth spectral moment, in simulation C (growing cloud). We note that this is feasible due to the relationship between column density and initialized cloud properties, explained in Section 3 ($R_{\rm cl} \propto \rho_{\rm cl}^{-1/3}$, $R_{\rm cl} \propto n_{\rm cl}^{1/3}$, $N_{\rm cl} \propto n_{\rm cl}^{2/3}$). As a result, after initial runs with simulations A and B, it is fairly simple to adjust initial conditions such as thermal pressure p/k_B and radius $R_{\rm cl}$ in order to approximately produce the desired values of $N_{\rm HI}$ in the initial conditions, but the fact that these clouds maintain these column densities over time is promising.

Intensity-weighted mean velocities (first spectral moment) and velocity dispersions (second moment) are more difficult to replicate. Mock observation velocity channels are initialized with their center at 0 km/s, and we shift the spectra by +80 km/s for comparison with observations. Therefore, when we compare $\overline{v}_{\rm LSR}$ of the Smith Cloud to mock observations, we focus on replicating the *spread* of $\overline{v}_{\rm LSR}$.

We were unable to fully match both the range of $\overline{v}_{\rm LSR}$ and the shape of the joint distributions involving it at our standard viewing angle of $\phi = 90°$. The mock observations, especially at later times, form more 'blobby' distributions in the velocity and velocity dispersion parameter space (Figure 6), with the center of the distribution around 80 km/s. Most mock observations also have velocity dispersions that are low compared to the Smith Cloud, though the overall distribution is similar (Figure 4). The simulations at $\phi = 90°$ have a narrower velocity range that does not seem to correlate strongly with velocity dispersion.

From Figure 10, decreasing the viewing angle ϕ to capture more of the cloud's bulk velocity shows promise in increasing the range of the line-of-sight velocity, similar to results from Henley et al. (2017). In addition, not only do viewing angles of $\phi = 30 - 60°$ better match the observed range of $\overline{v}_{\rm LSR}$, but these are a better match to the predicted angle of the Smith Cloud ($35 - 55°$; Lockman et al. 2008). By using angles closer to what is estimated by observations, we are able to reproduce the observed correlations with $\overline{v}_{\rm LSR}$ and $N_{\rm HI}$ in Figure 4. This orientation captures more of the simulated cloud's gradient (before $12t_{\rm cc}$), which is perhaps a hint as to the current dynamical state of the cloud.

Notably, we *are* able to largely match the column density – velocity dispersion distribution in Figure 5. This relationship, being common across all simulations and the observations, is a result of noise reduction methods. The sigma clipping removes all brightness temperature values below 3 standard deviations of an observational emission-free channel, meaning that line profiles with lower intensities (lower column densities after integration) are significantly truncated, only leaving the peak of the distribution and narrowing the velocity range. As a result, the velocity dispersion appears much smaller at lower column densities. Higher column densities are less affected, and keep more of their line profiles across wider velocity ranges, leading to an increased velocity dispersion. Therefore, the relationship between $N_{\rm HI}$ and $\overline{v}_{\rm LSR}$ is consistent across both the Smith Cloud and our simulation suite.

Despite the lack of an exact match in all parameters for the Smith Cloud, we elaborate on how patterns in these quantities may point to cloud evolution in Section 5.3. This is also likely influenced by several factors that we discuss further in Section 5.4, including the omission of gravity and limitation on the observations' velocity channels.

5.1.3 Projected First-Order Velocity Structure Function

Many of the projected first-order velocity structure functions of our simulations beyond $t = 3t_{\rm cc}$ are similar to what is observed with GALFA-HI (Figures 7 and 11).

Our closest match to the Smith Cloud is simulation C. It shows a good match at small separations, but, for our standard ($\phi = 90°$) viewing angle, the VSF flattens at large angles, which is not observed. However, the projected VSF at various viewing angles in Figure 11 shows that angles of $\phi = 30 - 60°$ do not exhibit this same flattening effect, instead becoming more similar to observations at later $t_{\rm cc}$, largely due to the inclusion of the cloud's bulk velocity along the line of sight. This distinction points to how both the small-scale turbulence within the cloud (low ℓ) and the large-scale motions (large ℓ) can be seen in the VCF.

Therefore, particularly when a cloud is growing and orientations are similar to what is quoted by Lockman et al. (2008), a VSF quite similar to observations can be replicated as the cloud evolves. We discuss further considerations of the VSF in Section 5.2.

5.1.4 Normalized Autocovariance Function

Even when varying simulation properties (metallicity, thermal pressure, cloud radius, and cooling) and mock observation parameters

(viewing angles and cloud distance), none presented here are able to provide a perfect match for the normalized autocovariance function of neutral hydrogen column density, $\Gamma(N_{\rm HI})$, as calculated by Equation 2. In particular, while we can get good agreement on sub-degree scales, the simulations systematically underpredict the large-scale autocovariance.

By comparing the observed and simulated autocovariance functions, we are able to hypothesize physical drivers that would better match the SC. First, recalling that $\Gamma(N_{\rm HI}) \approx 1$ near low ℓ indicates nearly perfect correlation in $N_{\rm HI}$ between the closest pairs of points, we therefore expect that a larger cloud would exhibit less variation in column density, or (equivalently) have $\Gamma(N_{\rm HI}) \approx 1$ for the same or larger ℓ than a smaller cloud. Similarly, if the function reaches a value of 0 around the cloud's radius, then this zero-point may indicate the cloud's size, indicating that a larger cloud can shift the ACF to larger scales.

It is not certain whether such clouds would have a similar slope to observations; we also note that the simulation initial conditions in this paper arise from an idealized scenario, such as a uniform cloud with constant velocity. It is possible that setting initial conditions from more physically motivated processes, such as generated by gravitational acceleration, may produce slopes similar to what is observed. However, we note that this is only applicable for high-intensity clouds that are less sensitive to sigma clipping, such as for our simulation C.

5.2 Interpreting the Observed Velocity Structure Function

In this paper, we characterize various scales of turbulence in the Smith Cloud and in our mock observations through the projected first-order velocity structure function (see also Chira et al. 2019; Ha et al. 2021; Gronke et al. 2022; Hu et al. 2022; Chen et al. 2023a; Abruzzo et al. 2024). While the VSF can be useful for measuring turbulence on different scales, these works discuss considerations when using projected velocity structure functions, as most theoretical expectations are established in three dimensions.

von Hoerner (1951) demonstrated that the shape of the VSF may depend on the line-of-sight (LOS) cloud depth. Known as projection smoothing, this affects the slope of the VSF for separations smaller than the LOS cloud depth. For example, while idealized Kolmogorov turbulence is expected to have a slope of $\ell^{1/3}$, a steeper slope in the projected VSF might be recovered, especially at low ℓ, with Kolmogorov turbulence being resolved at a higher ℓ (von Hoerner 1951; O'Dell & Castaneda 1987; Xu 2020; Mohapatra et al. 2022; Chen et al. 2023a). Li et al. (2020b) specifically argue that, in the context of galaxy clusters, the Kolmogorov slope is only recovered just before the turbulence driving scale. In this case, we do not expect to see Kolmogorov turbulence in these simulations due to underresolving the turbulent cascade (Abruzzo et al. 2024; Rennehan 2021; Mohapatra et al. 2022).

Furthermore, the VSF can indicate stages of cloud evolution. Because all of our simulated clouds begin as nearly uniform spheres with constant velocity, we might then expect VSFs to be similar at early times. Differences should appear as the cloud evolves, and they should correspond to the perceived cloud depth. Indeed, though our simulated clouds are slightly disrupted by the first cloud-crushing time, all early VSFs in Figure 7 are similar. Changes in the slope are visible around the relative size of the cloud, which is larger for simulations A and B than C and D. Clouds A and B remain similar up to $5t_{\rm cc}$, where A's higher metallicity causes the evolution to differ and entrain more wind material. At later times for growing clouds A and C, their slopes change or become unstable at $\ell < R_{\rm cl}$, possibly indicating a change in the distribution of LOS cloud depths.

As viewing angle — and therefore cloud depth — changes, so does the projection effect in Figure 11. As ϕ varies, so does the ℓ of the slope transition and steepness. Low ℓ is unaffected, as this region probes turbulence within the cloud. By $12t_{\rm cc}$ for all ϕ, the slope is more constant due to the coevolution of the cloud and bulk velocity. Similar to results by Abruzzo et al. (2024) using the three-dimensional second-order VSF, we also find that the driving scale, or the peak of the VSF, changes very little over cloud-crushing times (for a given angle of ϕ).

Finally, we find it essential to address a significant result from Chen et al. (2023a): spatial smoothing directly impacts the VSF, and is more significant for flatter intrinsic slopes. Because the VSF is measured on spatial scales, spatial smoothing in RA/DEC may result in decreased $\langle|\delta v_\perp|\rangle$ at lower ℓ, as velocity variations have been averaged over. This results in a steeper slope at low ℓ, where the intrinsic VSF is not recovered until the highest spatial separations, if at all. While we spatially convolute our mock observations in order to match the observational beam size, we agree with Chen et al. (2023a) in that any further spatial smoothing would result in better agreement at low ℓ, but that this would be an artifact of little meaning as opposed to a true match. Similarly, this means that neglecting to match the mock observations' beam size to GALFA-HI would result in more disagreement of the VSF. For future studies, it is essential for comparison of the VSF that beam size is identical between observations and simulations, and if further spatial convolution is used (which we discourage), this should be accounted for by either noting the affected scales or implementing the correction of the second-order VSF by Chen et al. (2023a).

5.3 Implications for Observers

We have shown a proof-of-concept demonstrating that, while not exactly matching the Smith Cloud, these comparison metrics may be used to investigate questions about observed clouds, including their evolutionary state, size, orientation, degree of turbulence, and their eventual fate. While it is difficult to use measurements at one point in time as a sole diagnostic for cloud survival, quantities in our mock observations appear to show several potentially useful patterns.

For example, growing clouds appear to have a slight drop in column density during entrainment, which later increases as the cloud accretes wind material. LOS velocity and velocity dispersion also show subtle variations depending on the cloud's stage of evolution. In simulation C, the ranges of $\bar{v}_{\rm LSR}$ and velocity dispersion increase as the cloud undergoes entrainment, then both decrease as the cloud continues growing.

The first-order projected VSF also provides observers with potential information about turbulence driving at different scales, and through the projection effect (or lack thereof), it may be possible to constrain a cloud's orientation with respect to the bulk velocity and/or the evolution of this velocity along the length of the cloud. In the case of the Smith Cloud, this is more likely represented by an orientation that captures part of this motion within the line of sight, such as $\phi = 30 - 60°$ at late times (suggesting a more evolved cloud) in Figure 11.

An additional metric of cloud depth or radius (for high-intensity clouds) may also be the normalized autocovariance function, where values of $\Gamma(N_{\rm HI}) \approx 1$ indicate an identical column density in the cloud at that particular separation ℓ. As described in Section 4.3, the cloud's size significantly affects this, as well as where the function reaches zero. This makes intuitive sense: a larger radius results in a

larger ℓ at which column densities are similar. For clouds that undergo steady growth, such as simulation C or both clouds in Appendix A, this function does not significantly evolve with cloud-crushing time, nor does it change with viewing angle, providing a more robust measurement. This metric may be more sensitive to HVC distance estimates, as the distance of a cloud affects the angular size ℓ on the sky.

5.4 Caveats and Considerations

As also noted in Abruzzo et al. (2024), there are several considerations to take into account for both simulations and observations.

From the simulation perspective, there are physical processes not implemented in the presented suite that may affect results such as cloud survival, radiative transfer, turbulence, and cloud morphologies. Perhaps the most significant missing physics is the implementation of gravity. At only ~3 kpc from the Galactic plane (Putman et al. 2003; Lockman et al. 2008), the Smith Cloud's proximity means a strong gravitational force, and it has been observed to be falling into the Galaxy at an observed rate of $v_z = 70$ km/s (Lockman et al. 2008). This provides an additional contribution to the cloud's overall velocity not simulated here, and as noted by Tan et al. (2023), can have a significant impact on turbulence (and, by extension, the VSF), $\overline{v}_{\rm LSR}$, and velocity dispersions. Gravitational acceleration may drive the observed joint distributions that we fail to replicate (Figures 4 & 6), as denser parts of the cloud will be less buoyant.

We also do not account for magnetic fields, which may defer (but not prevent) cloud destruction (Dursi & Pfrommer 2008; McCourt et al. 2015). Most relevant to this paper is their direct influence on turbulence, which Gronke & Oh (2020b) show may result in changes to cloud morphologies or lessening of hydrodynamical instabilities (e.g., Kelvin-Helmholtz) that propel mixing between the cloud and wind (Galyardt & Shelton 2016; Abruzzo et al. 2024). Self-shielding may also be relevant to reproducing observed column densities at lower pressures (Sander & Hensler 2021; Farber et al. 2022), and we acknowledge that the UV background from Haardt & Madau (2012) does not take into account the SC's proximity to the Milky Way. Finite resolution of the mock observations may also be something to consider: if a ray from radiative transfer encounters few cells ($R_{\rm cl}/\Delta x = 2, 4, 6$, *etc*), the resulting spectrum may be impacted.

Additional physics not included here are the possible presence of a dark matter halo (Quilis & Moore 2001; Nichols & Bland-Hawthorn 2009; Galyardt & Shelton 2016), cosmic rays (Butsky et al. 2020), thermal conduction (Sander & Hensler 2021), and additional sources of turbulence, particularly in the simulation's initial conditions.

Finally, we note that recent X-ray observations show that the MW's virial and supervirial CGM phases may have significantly enhanced metallicity, resulting in solar and supersolar abundances for some species (Das et al. 2019, 2021; Gupta et al. 2021). This could mean that HVCs such as the Smith Cloud are moving through a hot medium where TRML entrainment is even *more* important, as increased metallicities result in more efficient cooling.

On the observational side, the GALFA-HI data does not encompass the *entire* Smith Cloud, reaching a minimum declination of $\delta = -0.725°$, while the head of the cloud has been observed by Lockman et al. (2008) to reach $\delta \sim -2°$ (Section 2). Therefore, taking advantage of the much higher-resolution GALFA-HI data cubes results in the loss of part of the cloud. Upon imposing a similar limitation to the mock observations, we did not find any changes in our primary conclusions, which we find promising, though follow-ups with the lower-resolution data may prove beneficial.

In terms of the observed $\overline{v}_{\rm LSR}$ range of the Smith Cloud, some SC emission extends to velocity channels outside our imposed limit of ~75−130 km/s, potentially down to 50 km/s. However, as some previous literature (Stark et al. 2015; Minter et al. 2024), we use this approximate cut to avoid Galactic contamination from the ISM that is difficult to filter out, but still captures the bulk of the SC's emission.

We note that the origin of the Smith Cloud is uncertain, with suggestions ranging from hot halo condensation and infalling dwarf galaxies (Stark et al. 2015; Tepper-García & Bland-Hawthorn 2018) to a Galactic fountain (e.g., Fox et al. 2016; Marasco & Fraternali 2017; Alig et al. 2018) and metallicity has been suggested as a possible discriminator. If, as this work suggests, the Smith Cloud is actively cooling and accreting hot halo gas, this has the potential to significantly change its overall metallicity, as explored in Henley et al. (2017), meaning that the cloud and hot halo gas would be unlikely to have the same metallicity as we have simulated here. This topic should be addressed in detail in a future work.

6 CONCLUSIONS AND FUTURE WORK

In this paper, we present the first detailed comparison of an observed HVC (the Smith Cloud) to simulated clouds in the observational plane. To determine the simulations' ability to reproduce observations, we produced mock radio cubes and compared their column densities, average intensity-weighted LOS velocities, and intensity-weighted LOS velocity dispersions, characterized their degrees of turbulence through a projected first-order velocity structure function, and measured column densities across the clouds through a normalized autocovariance function.

Although no mock observations are a match across all metrics for the Smith Cloud, we were able to reproduce many, and we examined physical drivers of these quantities and how they vary with metallicity (more efficient cooling), thermal pressure, initial size, cloud orientation, and distance.

Our primary conclusions can be summarized as follows:

(i) The chosen statical measures (zero, first, and second HI moment joint distributions, along with projected velocity structure functions and column density autocovariance functions) are effective in qualitatively comparing simulated and observed cloud properties.

(ii) While many of our simulations reproduce the range of observed moments and naturally reproduce the observed correlation between the HI column density and the velocity dispersion (Figure 5), they generally do not reproduce the correlations between the other moments (Figure 4 and Figure 6). The exception is simulation C with viewing angles $\phi = 30 - 60°$.

(iii) Mock observations replicate the same range in average LOS velocity as seen in the Smith Cloud (Figure 6) with viewing angles of $\phi = 30 - 60°$, similar to observational predictions for the SC's angle. Cloud orientation has a significant impact on the LOS velocity and projected VSF (Figures 10 and 11)

(iv) Given our assumed cloud initial conditions, the simulations imply that turbulent radiative mixing layers (TRML) and the physics of TRML entrainment are *highly* relevant for HVCs, especially the Smith Cloud. This is key to match observed properties, such as the VSF (Figures 7 and 11). This is evident in the evolution of clouds A and B, for example, which are identical aside from metallicity.

(v) The projected VSF provides insight into cloud turbulence on small scales (low ℓ) and bulk motion on larger scales (high ℓ). The Smith Cloud maintains a nearly constant slope and extends to $\ell \sim 10°$, which simulation C only replicates at $\phi = 30 - 60°$. (Figures 7 and 11.)

(vi) No mock observations are a perfect match for the observed autocovariance function of column density on large scales. We suggest that the primary physical drivers of this function are the initial cloud size and whether the cloud is actively growing or being destroyed (see Figure 8).

With this paper showing that these concepts and statistics may be applied (and even replicated) across radio data cubes of observed HVCs and mock observations, further work on this topic is critical to understanding the key physics involved in predicting the fate of the Milky Way's HVCs: whether they will fuel our Galaxy's hot halo medium or provide a source for future star formation. However, such future revelations will require significant contributions from both observations and simulations.

Hundreds of HVCs have been observed in the Milky Way, providing a large observational sample size through which to extend these comparisons. Follow-up work with different HVCs, particularly those with high-resolution observations, will be necessary to understand the robustness of these statistics beyond just the Smith Cloud, and will ideally include HVCs in different environments, such as large complexes. Future simulations should include additional physics such as gravitational acceleration, magnetic fields, and self-shielding. In addition, we recommend that subsequent works test various initial cloud configurations, such as including velocity or metallicity gradients. These modifications may prove useful in better replicating the environments in which HVCs are formed and reside, potentially constraining HVC progenitors and determining how the properties of clouds are affected by the hot halo medium.

ACKNOWLEDGEMENTS

The authors thank the anonymous referee for providing suggestions that improved the quality of the manuscript. L.E.P. is grateful to David Schminovich, Frederik Paerels, and Kathryn Johnston for useful conversations about the work. Authors ran simulations and analysis using Frontera allocation AST20007, supported by the NSF and TACC. The authors acknowledge support from NSF through grant AST-2307693. GLB acknowledges support from the NSF (AST-2108470, AST-2307419), NASA TCAN award 80NSSC21K1053, and the Simons Foundation through the Learning the Universe Collaboration. This research made use of `yt` (Turk et al. 2011), `matplotlib` (Hunter 2007), `numpy` (Van Der Walt et al. 2011), and `scipy` (Virtanen et al. 2020).

DATA AVAILABILITY

The data supporting the plots within this article are available on reasonable request to the corresponding author.

REFERENCES

Abruzzo M. W., Bryan G. L., Fielding D. B., 2022, Astrophys. J., 925, 199
Abruzzo M. W., Fielding D. B., Bryan G. L., 2023, ArXiv eprints
Abruzzo M. W., Fielding D. B., Bryan G. L., 2024, Astrophys. J., 966, 181
Alig C., Hammer S., Borodatchenkova N., Dobbs C. L., Burkert A., 2018, Astrophys. J. Lett., 869, L2
Armillotta L., Fraternali F., Marinacci F., 2016, Mon. Not. R. Astron. Soc., 462, 4157
Balbus S., McKee C. F., 1982, Astrophys. J., 252, 529
Ben Bekhti N., Richter P., Winkel B., Kenn F., Westmeier T., 2009, Astron. Astrophys., 503, 483
Bordner J., Norman M. L., 2012, in BW-XSEDE'12 Proc. Extrem. Scaling Work.. Champaign, IL, pp 1–11
Bordner J., Norman M. L., 2018, ArXiv eprints
Brüns C., Kerp J., Kalberla P. M., Mebold U., 2000, Astron. Astrophys., 357, 120
Bryan G. L., et al., 2014, Astrophys. Journal, Suppl. Ser., 211
Bustard C., Gronke M., 2022, Astrophys. J., 933, 120
Butsky I. S., Fielding D. B., Hayward C. C., Hummels C. B., Quinn T. R., Werk J. K., 2020, Astrophys. J., 903, 77
Chen Z., Oh S. P., 2024, Mon. Not. R. Astron. Soc., 530, 4032
Chen M. C., et al., 2023a, Mon. Not. R. Astron. Soc., 518, 2354
Chen Z., Fielding D. B., Bryan G. L., 2023b, Astrophys. J., 950, 91
Chiappini C., Matteucci F., Romano D., 2001, Astrophys. J., 554, 1044
Chiappini C., Matteucci F., Meynet G., 2003, Astron. Astrophys., 410, 257
Chira R. A., Ibáñez-Mejía J. C., Mac Low M. M., Henning T., 2019, Astron. Astrophys., 630, 1
Chomiuk L., Povich M. S., 2011, Astron. J., 142
Cooper J. L., Bicknell G. V., Sutherland R. S., Bland-Hawthorn J., 2009, Astrophys. J., 703, 330
Das S., Mathur S., Nicastro F., Krongold Y., 2019, Astrophys. J. Lett., 882, L23
Das S., Mathur S., Gupta A., Krongold Y., 2021, Astrophys. J., 918, 83
Davé R., Anglés-Alcázar D., Narayanan D., Li Q., Rafieferantsoa M. H., Appleby S., 2019, Mon. Not. R. Astron. Soc., 486, 2827
Dursi L. J., Pfrommer C., 2008, Astrophys. J., 677, 993
Elia D., et al., 2022, Astrophys. J., 941, 162
Erb D. K., 2008, Astrophys. J., 674, 151
Farber R. J., Gronke M., Planck M., M D.-G., 2022, Mon. Not. R. Astron. Soc., 510, 551
Federrath C., 2013, Mon. Not. R. Astron. Soc., 436, 1245
Fielding D. B., Ostriker E. C., Bryan G. L., Jermyn A. S., 2020, Astrophys. J. Lett., 894, L24
Fox A. J., et al., 2014, Astrophys. J., 787
Fox A. J., et al., 2016, Astrophys. J. Lett., 816, L11
Fox A. J., Richter P., Ashley T., Heckman T. M., Lehner N., Werk J. K., Bordoloi R., Peeples M. S., 2019, Astrophys. J., 884, 53
Fraternali F., Marasco A., Armillotta L., Marinacci F., 2015, Mon. Not. R. Astron. Soc. Lett., 447, L70
Frisch U., 1995, Turbulence: The legacy of A.N. Kolmogorov. Cambridge University Press., Cambridge
Fuchs B., Jahrei H., Flynn C., 2009, Astron. J., 137, 266
Galyardt J., Shelton R. L., 2016, Astrophys. J. Lett., 816, L18
Gronke M., Oh S. P., 2018, Mon. Not. R. Astron. Soc. Lett., 480, L111
Gronke M., Oh S. P., 2020a, Mon. Not. R. Astron. Soc., 492, 1970
Gronke M., Oh S. P., 2020b, Mon. Not. R. Astron. Soc. Lett., 494, L27
Gronke M., Oh S. P., Ji S., Norman C., 2022, Mon. Not. R. Astron. Soc., 511, 859
Gupta A., Kingsbury J., Mathur S., Das S., Galeazzi M., Krongold Y., Nicastro F., 2021, Astrophys. J., 909, 164
Ha T., Li Y., Xu S., Kounkel M., Li H., 2021, Astrophys. J. Lett., 907, L40
Haardt F., Madau P., 2012, Astrophys. J., 746
Heitsch F., Putman M. E., 2009, Astrophys. J., 698, 1485
Heitsch F., Bartell B., Clark S. E., Peek J. E., Cheng D., Putman M., 2016, Mon. Not. R. Astron. Soc. Lett., 462, L46
Heitsch F., Marchal A., Miville-Deschênes M. A., Shull J. M., Fox A. J., 2022, Mon. Not. R. Astron. Soc., 509, 4515
Henley D. B., Gritton J. A., Shelton R. L., 2017, Astrophys. J., 837, 82
Hidalgo-Pineda F., Farber R. J., Gronke M., 2024, Mon. Not. R. Astron. Soc., 527, 135
Hill A. S., Haffner L. M., Reynolds R. J., 2009, Astrophys. J., 703, 1832
Holm-hansen C., Putman M. E., Kim D. A., 2025, Mon. Not. R. Astron. Soc., 536, 3507
Hopkins A. M., McClure-Griffiths N. M., Gaensler B. M., 2008, Astrophys. J., 682, L13
Hsu W. H., Putman M. E., Heitsch F., Stanimirović S., Peek J. E., Clark S. E., 2011, Astron. J., 141
Hu Y., Federrath C., Xu S., Mathew S. S., 2022, Mon. Not. R. Astron. Soc., 513, 2100

Hunter J. D., 2007, Comput. Sci. Eng., 9, 90
Ji S., Oh S. P., Masterson P., 2019, Mon. Not. R. Astron. Soc., 487, 737
Joung M. R., Bryan G. L., Putman M. E., 2012, Astrophys. J., 745
Kanjilal V., Dutta A., Sharma P., 2021, Mon. Not. R. Astron. Soc., 501, 1143
Kennicutt R. C., Evans N. J., 2012, Annu. Rev. Astron. Astrophys., 50, 531
Klein R., McKee C. F., Colella P., 1994, Astrophys. J., 420, 213
Larson R. B., Tinsley B., Caldwell N., 1980, Astrophys. J., 237, 692
Lehner N., Howk J. C., Marasco A., Fraternali F., 2022, Mon. Not. R. Astron. Soc., 513, 3228
Li Z., Hopkins P. F., Squire J., Hummels C., 2020a, Mon. Not. R. Astron. Soc., 492, 1841
Li Y., et al., 2020b, Astrophys. J. Lett., 889, L1
Li Y., Luo R., Fossati M., Sun M., J P., Occhialini F. G., 2023, Mon. Not. R. Astron. Soc., 521, 4785
Licquia T. C., Newman J. A., 2015, Astrophys. J., 806, 96
Lockman F. J., Benjamin R. A., Heroux A. J., Langston G. I., 2008, Astrophys. J., 679, L21
Maller A. H., Bullock J. S., 2004, Mon. Not. R. Astron. Soc., 355, 694
Marasco A., Fraternali F., 2017, Mon. Not. R. Astron. Soc. Lett., 464, L100
Marinacci F., Binney J., Fraternali F., Nipoti C., Ciotti L., Londrillo P., 2010, Mon. Not. R. Astron. Soc., 404, 1464
McCourt M., O'Leary R. M., Madigan A. M., Quataert E., 2015, Mon. Not. R. Astron. Soc., 449, 2
McKee C. F., Cowie L. L., 1977, Astrophys. J., 215, 213
Minter A. H., Lockman F. J., Balashev S. A., Ford H. A., 2024, Astrophys. J., 966, 76
Mohapatra R., Jetti M., Sharma P., Federrath C., 2022, Mon. Not. R. Astron. Soc., 510, 2327
Nichols M., Bland-Hawthorn J., 2009, Astrophys. J., 707, 1642
O'Dell C. R., Castaneda H. O., 1987, Astrophys. J., 317, 686
Oort J. H., 1969, Nature, 224, 1158
Ossenkopf V., Low M. M., 2002, Astron. Astrophys., 390, 307
Peek J. E. G., Putman M. E., McKee C. F., Heiles C., Stanimirović S., 2007, Astrophys. J., 656, 907
Peek J. E. G., et al., 2018, Astrophys. J. Suppl. Ser., 234, 2
Pillepich A., et al., 2018, Mon. Not. R. Astron. Soc., 473, 4077
Putman M. E., Bland-Hawthorn J., Veilleux S., Gibson B. K., Freeman K. C., Maloney P. R., 2003, Astrophys. J., 597, 948
Putman M. E., Peek J. E., Joung M. R., 2012, Annu. Rev. Astron. Astrophys., 50, 491
Quilis V., Moore B., 2001, Astrophys. J., 555, L95
Rennehan D., 2021, Mon. Not. R. Astron. Soc., 506, 2836
Richie H. M., Schneider E. E., Abruzzo M. W., Torrey P., 2024, Astrophys. J., 974, 81
Robitaille T. P., Whitney B. A., 2010, Astrophys. J. Lett., 710, 11
Sander B., Hensler G., 2021, Mon. Not. R. Astron. Soc., 501, 5330
Scannapieco E., Brüggen M., 2015, Astrophys. J., 805, 158
Schneider E. E., Robertson B. E., 2017, Astrophys. J., 834, 144
Sembach K. R., et al., 2003, Astrophys. J. Suppl. Ser., 146, 165
Smith G., 1963, Bull. Astron. Institutes Netherlands, 17, 203
Smith B. D., et al., 2017, Mon. Not. R. Astron. Soc., 466, 2217
Sparre M., Pfrommer C., Vogelsberger M., 2019, Mon. Not. R. Astron. Soc., 482, 5401
Sparre M., Pfrommer C., Ehlert K., 2020, Mon. Not. R. Astron. Soc., 499, 4261
Stanimirović S., et al., 2006, Astrophys. J., 653, 1210
Stark D. V., Baker A. D., Kannappan S. J., 2015, Mon. Not. R. Astron. Soc., 446, 1855
Tan B., Peng Oh S., Gronke M., 2021, Mon. Not. R. Astron. Soc., 502, 3179
Tan B., Oh S. P., Gronke M., 2023, Mon. Not. R. Astron. Soc., 520, 2571
Tepper-García T., Bland-Hawthorn J., 2018, Mon. Not. R. Astron. Soc., 473, 5514
Turk M. J., Smith B. D., Oishi J. S., Skory S., Skillman S. W., Abel T., Norman M. L., 2011, Astrophys. Journal, Suppl. Ser., 192
Van Der Walt S., Colbert S. C., Varoquaux G., 2011, Comput. Sci. Eng., 13, 22
Virtanen P., et al., 2020, Nat. Methods, 17, 261
Wakker B. P., van Woerden H., 1997, Annu. Rev. Astron. Astrophys., 35, 217

Table A1. Initial conditions of each simulation for a brief resolution study, including the density contrast $\chi = \rho_{\rm cl}/\rho_{\rm w}$, radius of the cloud ($R_{\rm cl}$), temperature of the wind ($T_{\rm w}$), and all resolutions included for that particular cloud in terms of $R_{\rm cl}/\Delta x$. Both simulations have thermal pressure $p/k_B = 10^3$ K cm^{-3}, Mach number $\mathcal{M} = 1.5$, and metallicity $Z_{\rm cl} = Z_\odot$. Clouds are named according to their density contrast in the first column (e.g., Cloud 100 has $\chi = 100$).

χ	$R_{\rm cl}$ [pc]	$T_{\rm w}$ [K]	$R_{\rm cl}/\Delta x$
100	56.38	3.28×10^5	4, 8, 16, 32
1000	864.70	3.28×10^6	4, 8, 16, 32, 64

Wakker B. P., Oosterloo T. A., Putman M. E., 2002, Astron. J., 123, 1953
Wakker B. P., York D. G., Wilhelm R., Barentine J. C., Richter P., Beers T. C., Ivezić Ž., Howk J. C., 2008, Astrophys. J., 672, 298
Xu S., 2020, Mon. Not. R. Astron. Soc., 492, 1044
Zhang D., Thompson T. A., Quataert E., Murray N., 2017, Mon. Not. R. Astron. Soc., 468, 4801
von Hoerner S., 1951, Zeitschrift für Astrophys., 30, 17

APPENDIX A: IMPACT OF SIMULATION RESOLUTION

Because simulation resolution has the potential to impact results we present here, we now investigate this using two simulated clouds in the suite presented by Abruzzo et al. (2024). Where the previously-shown simulations have a constant resolution of $R_{\rm cl}/\Delta x = 16$, the simulations in this Appendix now vary from $R_{\rm cl}/\Delta x = 4$ to $R_{\rm cl}/\Delta x = 64$. The properties of the clouds are presented in Table A1, where we note that each cloud (Cloud 100 and Cloud 1000) is referred to based on density contrast values χ. Because these simulations were not introduced by this paper with the intent of attempting to replicate the Smith Cloud, we do not match the GALFA-HI beam function, add noise, or use noise reduction methods outlined in Section 3.

Figure A1 shows the morphology for Cloud 100 over each moment (columns) with increasing resolution (rows) at $t/t_{\rm cc} = 4$. It is evident that the small, clump-like structures, often referred to as cloudlets, are most easily seen at the highest-resolution (bottom row). At lower resolutions, unresolved cloudlets appear to form a more linear tail, and deviations in column densities (first column) and $\overline{v}_{\rm LSR}$ (second column) are less obvious.

The projected velocity structure functions and normalized autocovariance functions of column density for Cloud 100 are both found in Figure A2, colored by $t/t_{\rm cc}$ as Figures 7 and 8. For the VSF, as resolution increases, the function appears to be vertically compressed to higher values and shows less variation. Increased resolution also shows larger values of $\langle|\delta v_\perp|\rangle$ at low ℓ, indicating that turbulence within the cloud is poorly resolved at $R_{\rm cl}/\Delta x = 4 - 8$, and larger resolutions are required to properly capture these scales. There is less variation in VSF values at high ℓ, pointing to the ability of the simulation to resolve the bulk velocity of the system.

Deviations in $\Gamma(N_{\rm HI})$ are more subtle, but the function appears to be smoother with increasing resolution, most visible at $7t_{\rm cc}$, which is almost completely flat for $\ell > 0.1$ at $R_{\rm cl}/\Delta x = 32$.

Similarly, Figure A3 displays the spatial moment distributions of the significantly larger Cloud 1000 at three cloud-crushing times, now with $R_{\rm cl}/\Delta x = 64$. At the lowest resolution of $R_{\rm cl}/\Delta x = 4$ (top row), the cloud appears to maintain much of its original spherical shape and uniform velocity, with a linear tail (as with Cloud 100 in Figure A1) being visible. Perturbations become more obvious with

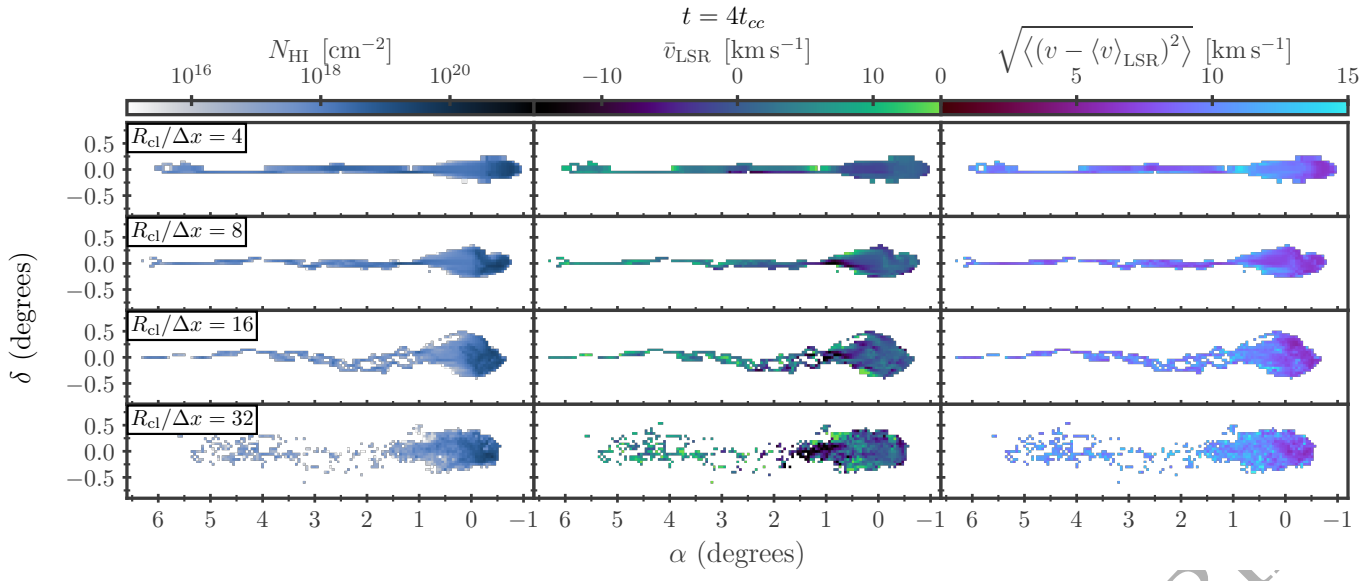

Figure A1. Moment maps of Cloud 100, with rows organized by resolution and columns as each moment, similar to Figures 2 and 3, at $4t_{\rm cc}$. Small-scale structures, such as individual clumps in the cloud-wind interaction, are most identifiable at $R_{\rm cl}/\Delta x = 32$. At lower resolutions, the cloud forms a nearly linear tail that is longer than at the highest resolution (bottom row). While subtle, the decreasing column densities in the tail of the cloud, as well as the extent of the velocity variations, are not as evident at lower resolutions.

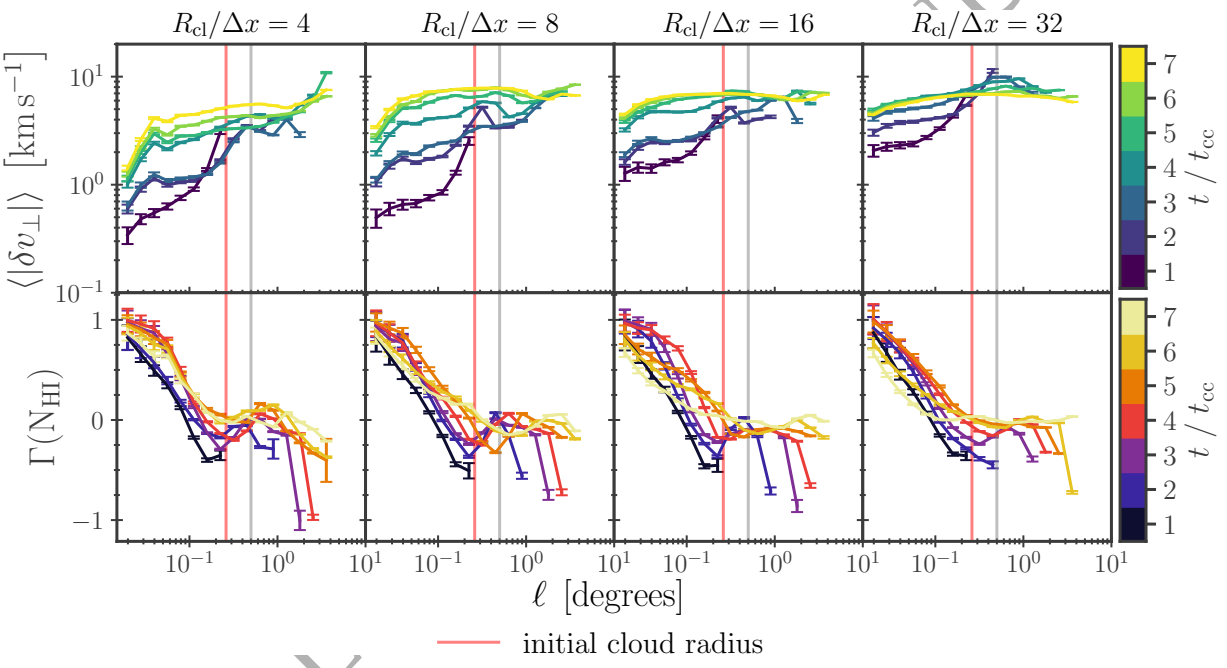

Figure A2. Projected first-order velocity structure function (top row) and normalized autocovariance function of column density (bottom row), colored by cloud-crushing times up to $t/t_{\rm cc} = 7$, for Cloud 100. As Figures 7 and 8, the vertical grey line serves as a point of reference for $\ell = 0.5°$, and the vertical red line is the cloud's initial radius. Resolution increases with each column, with the left column showing the lowest resolution ($R_{\rm cl}/\Delta x = 4$) and the right column having the highest resolution ($R_{\rm cl}/\Delta x = 32$). Increasing resolution appears to shift the velocity structure function to larger values of $\langle |\delta v_\perp| \rangle$, and results in less variation at later cloud-crushing times. $\Gamma(N_{\rm HI})$ tends to flatten slightly with increasing resolution, particularly at later times.

increasing resolution, where structure begin to form at the head and tail of the cloud. This is best seen at the highest resolutions (bottom two rows) where the cloud structure becomes much more complex. Again, the lowest resolutions do not capture the same deviations in each property that are visible at the highest resolution.

Finally, Figure A4 is the projected VSF and normalized ACF of neutral hydrogen column density for Cloud 1000. The variations in the VSF with resolution are the same as found in Cloud 100: the VSF appears to be vertically compressed with increasing resolution as values at low ℓ are significantly affected . We note that this variation in the projected first-order VSF is likely related to when each respective simulation is able to resolve significant variations in $\bar{v}_{\rm LSR}$, as the VSF

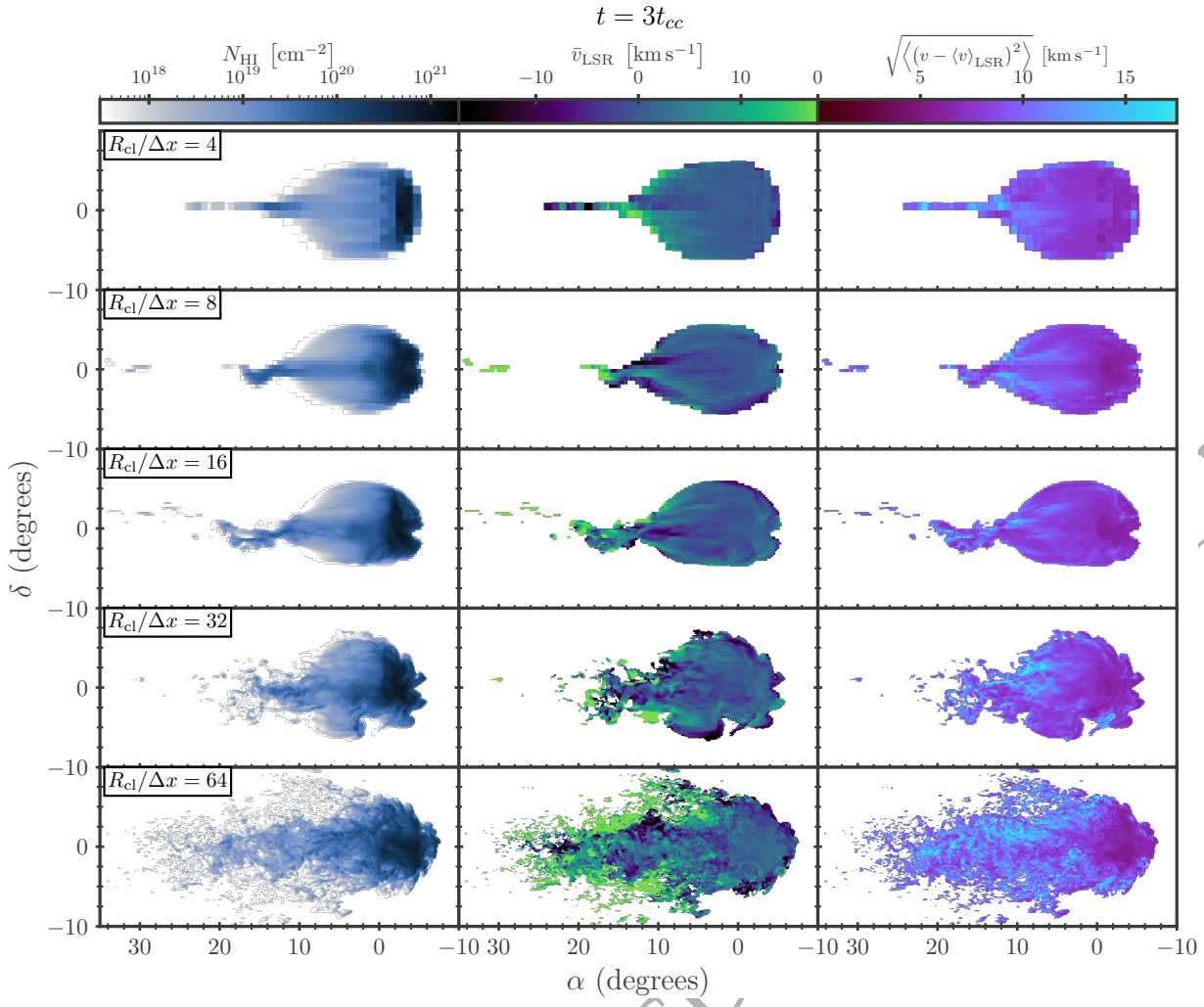

Figure A3. Same as Figure A1, but for Cloud 1000 at $3t_{cc}$. We note that, from Cloud 100, the minimum column density (first column) colorbar has been increased by about 100 cm^{-2}, and mean velocity (second column) has been increased by about ±3 km/s. As with Figure A1, small-scale structures within the cloud become more visible with higher resolution.

is calculated from this parameter; increased resolution means that the simulation is able to better resolve small-scale turbulence.

The normalized autocovariance function of column density, $\Gamma(N_{HI})$, appears in the bottom row of Figure A4. Again like Cloud 100, Cloud 1000 shows subtle dependence on resolution that is less quantifiable than the VSF.

While we caution that direct comparisons between the Smith Cloud and Clouds 100 and 1000 cannot be drawn, as they were not simulated with the intent of doing so and are not treated the exact same (with respect to convolution, noise, and noise reduction methods), they may provide further support to our conclusion that the shape of $\Gamma(N_{HI})$ is dependent on *both* (1) whether the cloud survives or not, and (2) the cloud's initial radius. Cloud 100, with an extremely small radius of $R_{\rm cl} \sim 56$ pc, has a function that immediately decreases from unity, showing an opposite trend to the Smith Cloud GALFA-HI observations, despite the fact that the cloud is not destroyed by $7t_{cc}$. Cloud 1000, on the other hand, has the largest radius, $R_{\rm cl} \sim 865$ pc, nearly twice that of simulations A and B, and the values of $\Gamma(N_{HI})$ are almost identical to the distribution of the Smith Cloud.

This aligns with predictions by Cooper et al. (2009), who suggest that radiative clouds are fragmented into smaller cloudlets that have the potential to form a filamentary structure if the cloud survives. Specifically, they predict that increased resolution results in more cloudlets (as visible in Figure A1) as the Kelvin-Helmholtz instability is further resolved.

Consequently, higher resolutions are needed to distinguish fine structures in neutral hydrogen, especially at earlier times and in the tail of the cloud. Lower resolution results in more linear clouds with less detail in the velocities. As a result, the VSF is also resolution-dependent: because we suggest that the VSF at small separations is descriptive of turbulence within the cloud, these scales must be adequately resolved, and can influence the shape of the function at low ℓ.

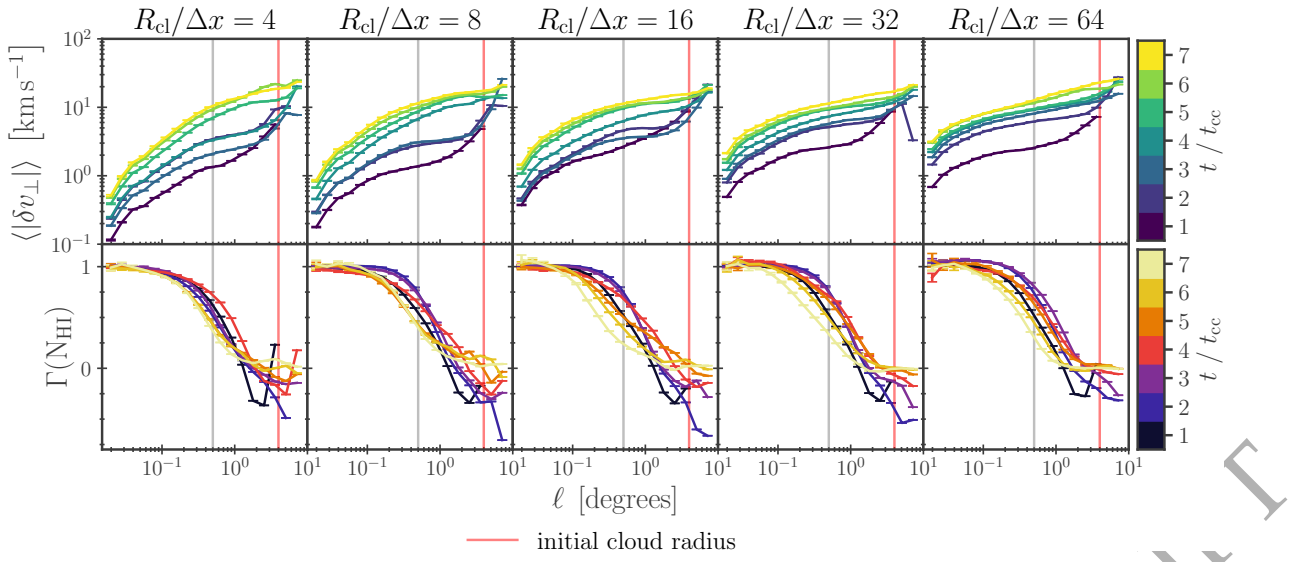

Figure A4. Same as Figure A2 for our second resolution study simulation, Cloud 1000, where the highest resolution is now $R_{cl}/\Delta x = 64$. Increasing resolution appears to cause the VSF the converge at $t/t_{cc} > 1$, increasing to larger values at smaller separations, resulting in the function shifting upwards. In contrast, $\Gamma(N_{HI})$ has little difference over time with $R_{cl}/\Delta x = 4$.